

Damped kink motions in a system of two solar coronal tubes with elliptic cross-sections

Mijie Shi¹, Bo Li¹, Shaoxia Chen¹, Hui Yu¹, and Mingzhe Guo^{1,2}

¹ Shandong Provincial Key Laboratory of Optical Astronomy and Solar-Terrestrial Environment, Institute of Space Sciences, Shandong University, Weihai 264209, China
e-mail: bbl@sdu.edu.cn

² Centre for Mathematical Plasma Astrophysics, Department of Mathematics, KU Leuven, Celestijnenlaan 200B, B-3001 Leuven, Belgium

Received / Accepted

ABSTRACT

Aims. This study is motivated by observations of coordinated transverse displacements in neighboring solar active region loops, addressing specifically how the behavior of kink motions in straight two-tube equilibria is impacted by tube interactions and tube cross-sectional shapes.

Methods. We work with linear, ideal, pressureless magnetohydrodynamics. Axially standing kink motions are examined as an initial value problem for transversely structured equilibria involving two identical, field-aligned, density-enhanced tubes with elliptic cross-sections (elliptic tubes). Continuously nonuniform layers are implemented around both tube boundaries. We numerically follow the system response to external velocity drivers, largely focusing on the quasi-mode stage of internal flows to derive the pertinent periods and damping times.

Results. The periods and damping times we derive for two-circular-tube setups justify available modal results found with the T-matrix approach. Regardless of cross-sectional shapes, our nonuniform layers feature the development of small-scale shears and energy accumulation around Alfvén resonances, indicative of resonant absorption and phase-mixing. As with two-circular-tube systems, our configurational symmetries make it still possible to classify lower-order kink motions by the polarization and symmetric properties of the internal flows; hence such mode labels as S_x and A_x . However, the periods and damping times for two-elliptic-tube setups further depend on cross-sectional aspect ratios, with A_x motions occasionally damped less rapidly than S_x motions. We find uncertainties up to $\sim 20\%$ ($\sim 50\%$) for the axial Alfvén time (the inhomogeneity lengthscale) if the periods (damping times) computed for two-elliptic-tube setups are seismologically inverted with canonical theories for isolated circular tubes.

Conclusions. The effects of loop interactions and cross-sectional shapes need to be considered when the periods and particularly the damping times are seismologically exploited for coordinated transverse displacements in adjacent coronal loops.

Key words. magnetohydrodynamics (MHD) — Sun: corona — Sun: magnetic fields — waves

1. Introduction

Cyclic transverse displacements of solar coronal loops are arguably the most extensively observed collective motion in modern solar coronal seismology (see e.g., Nakariakov & Kolotkov 2020; Nakariakov et al. 2021, for recent reviews). Two regimes have been established. The decayless regime is such that the displacements show little damping and their magnitudes are usually substantially smaller than visible loop widths, with both features already clear when this regime was first identified in measurements with Hinode (Tian et al. 2012) and the Solar Dynamics Observatory/Atmospheric Imaging Assembly (SDO/AIA; Wang et al. 2012; Nisticò et al. 2013; Anfinogentov et al. 2013). This regime is known not to be connected with eruptive events but ubiquitous in active region (AR) loops, as evidenced by a statistical survey of the SDO/AIA data (Anfinogentov et al. 2015) and by the recent series of analyses of the measurements with the Extreme Ultraviolet Imager (EUI) on board the Solar Orbiter (e.g., Zhong et al. 2022; Petrova et al. 2023; Zhong et al. 2023). Decaying loop displacements, on the other hand, typically damp over several cycles and are of larger amplitudes as revealed by their first imaging observations by the Transition Region and Coronal Explorer (TRACE; Schrijver et al. 1999; Aschwanden et al. 1999; Nakariakov et al. 1999). These decaying motions are usually associated with lower coronal eruptions (Zimovets & Nakariakov 2015). Regardless, there exist ample detections of decaying displacements, an inexhaustive list being those by Hinode (Ofman & Wang 2008; Van Doorselaere et al. 2008a; Erdélyi & Taroyan 2008), the Solar TERrestrial RELations Observatories (STEREO; Verwichte et al. 2009), and by SDO/AIA (Aschwanden & Schrijver 2011; White & Verwichte 2012). Statistical studies therefore prove possible either through compiling published results (e.g., Verwichte et al. 2013) or via directly cataloging the SDO/AIA events (Goddard et al. 2016; Nechaeva et al. 2019). Decaying cyclic displacements were specifically established to be nearly exclusively axial fundamentals (e.g., Fig.9 in Goddard et al. 2016 and Fig.5 in Nechaeva et al. 2019).

Seismological applications of cyclic transverse displacements typically start with their identification as trapped fast kink motions. Practically, this identification largely relies on the scheme for classifying collective motions in straight, static, field-aligned

configurations where isolated density-enhanced tubes with circular cross-sections (circular tubes hereafter) are embedded in an otherwise uniform corona (Edwin & Roberts 1983, ER83; also Zajtsev & Stepanov 1975; Cally 1986). That the configuration is structured only transversely and in a one-dimensional (1D) manner means that the azimuthal wavenumber m makes physical sense, with kink motions corresponding to $m = 1$ (see the textbooks by Roberts 2019 and Goedbloed et al. 2019). Let “ER83 equilibria” label specifically those where the transverse structuring is piecewise constant. The relevant theories then enable the measured periods of axially standing kink motions to be employed to infer the axial Alfvén time and hence the coronal magnetic field strength for decayless (e.g., Anfinogentov & Nakariakov 2019; Li & Long 2023) and decaying regimes alike (Nakariakov & Ofman 2001; also the reviews by e.g., Nakariakov & Verwichte 2005; De Moortel & Nakariakov 2012; Nakariakov et al. 2021). While undamped for ER83 equilibria, trapped fast kink motions are in general resonantly absorbed in the Alfvén continuum when the 1D structuring is allowed to be continuous (Ruderman & Roberts 2002; Goossens et al. 2002, and references therein). Theoretically, the concept of kink quasi-modes then arises and the internal kink motions are damped in conjunction with the accumulation and phase-mixing of localized Alfvénic motions (e.g., Poedts & Kerner 1991; Tirry & Goossens 1996; Soler et al. 2013; also the review by Goossens et al. 2011). Seismologically, resonant absorption has been customarily invoked to interpret the decay of large-amplitude loop displacements, thereby allowing the measured damping times to be employed to deduce such key parameters as the transverse inhomogeneity lengthscales (e.g., Aschwanden et al. 2003; Goossens et al. 2008; Arregui & Asensio Ramos 2011; Arregui et al. 2015; Arregui 2022).

Deviations from the canonical ER83 equilibria are known to impact the behavior of collective motions, and we choose to focus on two geometrical properties that render the meaning of the azimuthal wavenumber not as clear (e.g., the review by Li et al. 2020). One concerns loop cross-sections, which may actually be tied to coronal heating via their key role in determining the morphology of coronal loops in, say, soft X-ray (Klimchuk et al. 1992) and EUV (Watko & Klimchuk 2000) in the first place. Recent imaging observations with Hi-C (Klimchuk & DeForest 2020) and Hi-C 2.1 (Williams et al. 2021) suggest that AR loops may maintain a circular cross-section throughout their visible segments. However, there also exist suggestions that favor elliptic cross-sections to better account for the morphology of AR loops, as deduced with the aid of coronal magnetic field modeling (e.g., Wang & Sakurai 1998; Malanushenko & Schrijver 2013) and/or multi-vantage-point measurements with STEREO (e.g., McCarthy et al. 2021). In particular, the derived aspect ratios may readily attain $\sim 1.5 - 5$ (Malanushenko & Schrijver 2013), a range also compatible with the spectroscopic measurements with Hinode/EUV Imaging Spectrometer (EIS; Kucera et al. 2019). Restrict ourselves to straight configurations where coronal loops preserve a constant elliptic cross-section along their axes (elliptic tubes hereafter). Substantial attention has been paid to collective perturbations in such equilibria from both the modal (e.g., Ruderman 2003; Erdélyi & Morton 2009; Morton & Ruderman 2011; Aldhafeeri et al. 2021) and initial-value-problem (IVP) perspectives (Guo et al. 2020). Despite the lack of axisymmetry, kink motions remain identifiable as those that transversely displace the tube axes, and in general they remain subjected to resonant absorption for continuous transverse structuring. However, as was first shown by Ruderman (2003), one now needs to discriminate two distinct polarizations, where the internal flows are primarily directed along the major (“major-polarized” for brevity) and minor axes (“minor-polarized”), respectively. In addition, the periods of major-(minor-) polarized kink motions increase (decrease) with the major-to-minor-axis ratio, while the damping times for both polarizations tend to increase with this ratio. It was further demonstrated that the density contrast between elliptic tubes and their surrounding fluids plays a subtle role in mediating the differences between the dispersive properties of the differently polarized motions (Guo et al. 2020).

Another geometrical property pertains to systems involving multiple tubular structures. Observationally, it has long been known that perturbations in such systems may evolve collectively, an incomplete list of examples being the coordinated transverse displacements detected either in groups of prominence threads (e.g., Yi et al. 1991; Lin et al. 2003; Okamoto et al. 2007; also the review by Arregui et al. 2018) or in neighboring AR loops (e.g., Schrijver & Brown 2000; Schrijver et al. 2002; Verwichte et al. 2004; Wang et al. 2012; White et al. 2013). Kink motions in straight multi-circular-tube systems have also been extensively examined theoretically. We choose to concentrate on the modal analyses where a harmonic time-dependence is assumed a priori, noting that multi-dimensional IVP studies prove equally informative (e.g., Terradas et al. 2008b; Ofman 2009; Magyar & Van Doorselaere 2016; Guo et al. 2019a). The first modal examination was due to Luna et al. (2008, hereafter L08), who numerically solved the pertinent eigenvalue problem (EVP) for undamped kink modes in a two-tube system. Broadly speaking, two different approaches have been employed in further modal studies. The ensuing EVPs turn out to be analytically tractable in the thin-tube (TT) limit for two-tube equilibria when formulated in bi-cylindrical coordinates, for both undamped (Van Doorselaere et al. 2008b; Robertson et al. 2010; Ruderman & Petrukhin 2023) and damped kink motions (Robertson & Ruderman 2011; Gijzen & Van Doorselaere 2014). Similar EVPs have also been formulated with the T-matrix formalism of scattering theory, originally introduced to solar contexts by Bogdan & Zweibel (1985, 1987). This formalism is sufficiently general for examining kink motions in composite equilibria comprising an arbitrary number of circular tubes, with specific investigations available for undamped motions in systems with two or three (Luna et al. 2009) up to tens of tubes (Luna et al. 2010, 2019). Addressing continuous transverse structuring, the T-matrix approach proves capable of handling the resonant absorption of collective motions in general (Keppens et al. 1994) and particularly that of kink motions in two-tube equilibria (Soler & Luna 2015, SL15 hereafter). The damping is nonetheless assumed to be weak by construction, given that it was incorporated in the T-matrix framework exclusively via the thin-boundary (TB) connection formulae (see SL15 for more details; also see Sakurai et al. 1991 for the first derivation of the TB formulae). Regardless, kink motions are known to be much more complicated in multi-tube equilibria than for isolated circular tubes, and we restrict ourselves to two-identical-tube systems. It was shown by L08 (see Fig.2 therein) that kink motions, namely those that displace both tube axes, need to be classified according to both the polarization and symmetric properties of the two internal flows. The notions of S_x , A_x , S_y , and A_y then ensue, one subtlety being that the $S_x - A_y$ and $A_x - S_y$ pairs become indistinguishable in terms of frequencies (Van Doorselaere et al. 2008b) and damping rates (SL15) when the tubes are sufficiently thin. This subtlety notwithstanding, A_x motions always turn out to oscillate and damp more rapidly than S_x motions: the differences between the frequencies and particularly the damping rates may be substantial enough to impact seismological deductions (see Fig.4 in SL15).

This study is intended to examine damped lower-order kink motions in a two-identical-elliptic-tube system, thereby addressing the situation where neither the equilibrium configuration as a whole nor an individual tube allows the azimuthal wavenumber to make exact sense. We will adopt linear, pressureless, ideal magnetohydrodynamics (MHD) throughout, given that quiescent AR loops are of primary interest. We will adopt an IVP perspective, paying particular attention to the frequencies and damping rates of axially standing motions by largely focusing on the duration where the concept of quasi-modes applies. Our study is new in the following two aspects. Firstly, two-elliptic-tube systems have yet to be explored in the context of collective waves, meaning that our study will shed new light on how the dispersive properties of kink motions are impacted by the joint effects of tube interactions and tube cross-sectional shapes. When put to seismological contexts, our results can therefore help assess the uncertainties in the key physical parameters that one deduces with the customary practice where the joints effects are absent. Secondly, there exist no IVP studies dedicated to the dispersive properties of damped kink motions in two-tube systems to our knowledge. Our numerical analysis, conducted with a self-developed code, will therefore help verify the T-matrix results obtained by SL15.

The outline of this manuscript is as follows. Section 2 offers the mathematical formulation of our IVP together with a description of our numerical code. We then focus on circular tubes in Sect.3, testing our code outputs against available results obtained with independent approaches. Section 4 proceeds to present our numerical results for two-elliptic-tube systems. Section 5 discusses some seismological implications of this study. Our findings are summarized in Sect. 6, where some concluding remarks are also given.

2. Problem Formulation and Solution Method

2.1. Governing Equations

We adopt pressureless, ideal MHD as our theoretical framework, in which the primitive dependents are the mass density ρ , velocity \mathbf{v} , and magnetic field \mathbf{B} . Let (x, y, z) be a Cartesian system, and let the equilibrium quantities be denoted with a subscript 0. We take the equilibrium magnetic field to be uniform and z -directed ($\mathbf{B}_0 = B_0 \mathbf{e}_z$). Only straight, static, field-aligned configurations are of interest, meaning that $\mathbf{v}_0 = 0$ and the structuring is encapsulated in $\rho_0(x, y)$. The Alfvén speed v_A is defined by $v_A^2 = B_0^2 / \mu_0 \rho_0$, where μ_0 is the magnetic permeability of free space. With magnetically closed structures in mind, we place two dense photospheres at $z = 0$ and $z = L$.

We formulate an IVP to examine how our equilibrium responds to small-amplitude perturbations (denoted by subscript 1). It follows from linearized, ideal, pressureless MHD equations that

$$\rho_0 \frac{\partial v_{1x}}{\partial t} = \frac{B_0}{\mu_0} \left(\frac{\partial B_{1x}}{\partial z} - \frac{\partial B_{1z}}{\partial x} \right), \quad (1)$$

$$\rho_0 \frac{\partial v_{1y}}{\partial t} = \frac{B_0}{\mu_0} \left(\frac{\partial B_{1y}}{\partial z} - \frac{\partial B_{1z}}{\partial y} \right), \quad (2)$$

$$\frac{\partial B_{1x}}{\partial t} = B_0 \frac{\partial v_{1x}}{\partial z}, \quad (3)$$

$$\frac{\partial B_{1y}}{\partial t} = B_0 \frac{\partial v_{1y}}{\partial z}, \quad (4)$$

$$\frac{\partial B_{1z}}{\partial t} = -B_0 \left(\frac{\partial v_{1x}}{\partial x} + \frac{\partial v_{1y}}{\partial y} \right). \quad (5)$$

We focus on axially standing motions by adopting the ansatz

$$\begin{aligned} v_{1x}(x, y, z; t) &= \hat{v}_x(x, y; t) \sin(kz), \\ v_{1y}(x, y, z; t) &= \hat{v}_y(x, y; t) \sin(kz), \\ B_{1x}(x, y, z; t) &= \hat{B}_x(x, y; t) \cos(kz), \\ B_{1y}(x, y, z; t) &= \hat{B}_y(x, y; t) \cos(kz), \\ B_{1z}(x, y, z; t) &= \hat{B}_z(x, y; t) \sin(kz), \end{aligned} \quad (6)$$

where $k = n\pi/L$ is the quantized axial wavenumber ($n = 1, 2, \dots$). Equations (1) to (5) then become

$$\frac{\partial \hat{v}_x}{\partial t} = -\frac{B_0}{\mu_0 \rho_0} \left(k \hat{B}_x + \frac{\partial \hat{B}_z}{\partial x} \right), \quad (7)$$

$$\frac{\partial \hat{v}_y}{\partial t} = -\frac{B_0}{\mu_0 \rho_0} \left(k \hat{B}_y + \frac{\partial \hat{B}_z}{\partial y} \right), \quad (8)$$

$$\frac{\partial \hat{B}_x}{\partial t} = k B_0 \hat{v}_x, \quad (9)$$

$$\frac{\partial \hat{B}_y}{\partial t} = k B_0 \hat{v}_y, \quad (10)$$

$$\frac{\partial \hat{B}_z}{\partial t} = -B_0 \left(\frac{\partial \hat{v}_x}{\partial x} + \frac{\partial \hat{v}_y}{\partial y} \right). \quad (11)$$

Axial fundamentals ($k = \pi/L$) will be examined throughout, even though our analysis can be readily adapted to any axial harmonic number n .

2.2. Energy Conservation Law

Energetics considerations turn out to be necessary. Consider a volume V that laterally occupies an arbitrary area Q and is axially bounded by the planes $z = 0$ and $z = L$. Let the curve enclosing Q be denoted by ∂Q . Let $[\mathbf{e}_n, \mathbf{e}_t, \mathbf{e}_z]$ further define a right-handed set of orthonormal system at any point along ∂Q , with the normal direction \mathbf{e}_n pointing away from Q . An energy conservation law can be readily derived from Eqs. (1) to (5), reading

$$\frac{dE(t)}{dt} = -F(t), \quad (12)$$

where

$$E(t) = \int_Q \epsilon dx dy, \quad (13)$$

$$F(t) = \oint_{\partial Q} dl_t \mathbf{e}_n \cdot \hat{\mathbf{p}}_T (\hat{v}_x \mathbf{e}_x + \hat{v}_y \mathbf{e}_y), \quad (14)$$

$$\epsilon(x, y; t) = \frac{1}{2} \rho_0 (\hat{v}_x^2 + \hat{v}_y^2) + \frac{1}{2\mu_0} (\hat{B}_x^2 + \hat{B}_y^2 + \hat{B}_z^2). \quad (15)$$

Note that the ansatz (6) has been employed, and $\hat{\mathbf{p}}_T = B_0 \hat{B}_z / \mu_0$ is connected with the Eulerian perturbation of total pressure. Note also that dl_t denotes the elementary arclength in the tangential direction defined by \mathbf{e}_t . When multiplied by $L/2$, the symbols E and F represent the instantaneous perturbation energy in V and the net energy flux out of V , respectively. We nonetheless refer to E (F) as the total energy (the net energy flux) for brevity. Likewise, the symbol ϵ in Eqs. (13) and (15) will be referred to as the energy density. We also drop the hat from here onward.

2.3. Equilibrium Configuration and Initial Perturbation

Our equilibrium comprises a composite structure embedded in an otherwise uniform external corona (denoted by subscript e). By “composite” we mean two identical tubes with elliptic cross-sections and separated by d . Let j label a tube, and let a 2D position vector $\mathbf{X}_j = (X_j, Y_j)$ denote the center of tube j . The tube centers are placed on the x -axis without loss of generality, enabling a tube to be referred to as either the left ($j = L$) or the right tube ($j = R$). The tube centers are further taken to be symmetric about $x = 0$, resulting in $X_{L,R} = \mp d/2$ and $Y_{L,R} = 0$. We consistently use subscript i to denote the equilibrium quantities at either tube axis, meaning in particular that the internal density and Alfvén speed are denoted by ρ_i and v_{Ai} , respectively. Likewise, by v_{Ae} we denote the Alfvén speed evaluated with the external density ρ_e .

Our two-tube structure is characterized as follows. The tubes are taken to be identical not only in cross-sectional shapes but in their orientations relative to the x -axis. For simplicity, we consider only two orientations by discriminating whether the major (hereafter “ x -major”) or minor axis (“ x -minor”) of a tube aligns with the x -direction. Let a_x and a_y denote the spatial extent that a tube spans in the x - and y -directions, respectively. The x -major (x -minor) orientation then means that $a_x > a_y$ ($a_x < a_y$). Both orientations are realized by the density distribution ($j = L$ or R),

$$\rho_j(x, y) = \begin{cases} \rho_i, & 0 \leq \bar{r}_j \leq 1 - \bar{l}; \\ \frac{\rho_i + \rho_e}{2} - \frac{\rho_i - \rho_e}{2} \cos \frac{\pi(\bar{r}_j - 1)}{\bar{l}}, & 1 - \bar{l} \leq \bar{r}_j \leq 1, \end{cases} \quad (16)$$

with the intermediate dimensionless variable \bar{r}_j defined by

$$\bar{r}_j(x, y) := \sqrt{\left(\frac{x - X_j}{a_x}\right)^2 + \left(\frac{y}{a_y}\right)^2}. \quad (17)$$

We take $d \geq 2a_x$ such that tube j can be unambiguously identified as where $\bar{r}_j \leq 1$. We also use a (b) to denote the semi-major (semi-minor) axis, meaning that $[a_x = a, a_y = b]$ ($[a_x = b, a_y = a]$) for the x -major (x -minor) orientation. The symbol b will be favored when the limiting case of circular tubes is examined ($a = b$). Equation (16) represents a tube profile that continuously connects the internal density ρ_i to the external one ρ_e via some elliptic layer of width $\bar{l}a$ ($\bar{l}b$) along the direction of the major (minor) axis. When $a = b$, this profile is equivalent to the sinusoidal distribution introduced by Ruderman & Roberts (2002, hereafter RR02) for modeling circular inhomogeneities (see e.g., Van Doorselaere et al. 2004; Soler et al. 2013; Chen et al. 2021, for more applications). Somehow subtle is that the RR02 implementation for a tube centered at $(X_j, 0)$ writes

$$\rho_j(x, y) = \begin{cases} \rho_i, & r_j \leq \mathcal{R} - \ell/2; \\ \frac{\rho_i + \rho_e}{2} - \frac{\rho_i - \rho_e}{2} \sin \frac{\pi(r_j - \mathcal{R})}{\ell}, & \mathcal{R} - \ell/2 \leq r_j \leq \mathcal{R} + \ell/2, \\ \rho_e, & r_j \geq \mathcal{R} + \ell/2. \end{cases} \quad (18)$$

Here $r_j := \sqrt{(x - X_j)^2 + y^2}$. Evidently, the geometrical parameters $[\mathcal{R}, \ell]$ characterizing the RR02 implementation are connected to ours via

$$b = \mathcal{R} + \ell/2,$$

$$\bar{l} = \frac{\ell}{b} = \frac{\ell/\mathcal{R}}{1 + \ell/2\mathcal{R}}. \quad (19)$$

Our equilibrium configuration, illustrated in Fig. 1b, is a straightened version of a composite system where two tubes are separated in the x -direction and anchored in the photosphere (Fig. 1a). We see the x - (y -) direction in Fig. 1b as horizontal (vertical) given that the $y - z$ plane can be identified as the tube plane. For two-tube systems, however, it turns out to be also necessary to classify lower-order kink motions into the S_x , A_x , S_y , and A_y types by combining the symmetric and polarization properties of the internal flow fields (see Fig. 2 in L08). Proposed for two-identical-circular-tube systems, the subscript x (y) arises when the internal velocities are dominated by their x - (y -) components, while the symbol S (A) is such that the dominant internal velocity component is symmetric (anti-symmetric) about $x = 0$. This classification is expected to carry over when elliptic tubes are examined. Somehow complicated is that one needs to distinguish between the x -major and x -minor arrangements (Figs. 1c and 1d), meaning for instance that the frequencies of the S_x motions are likely to be different for different tube orientations.

Our equilibrium is perturbed via velocities. We consider only S_x and A_x motions, given that kink motions are commonly observed to be horizontally polarized (see Zhong et al. 2023 and references therein; see e.g., Wang et al. 2008 and Aschwanden & Schrijver 2011 for observational instances of vertical kink motions). Regardless of tube orientations, these are excited by imposing

$$\frac{v_{\text{ini}}(x, y)}{v_{\text{Ae}}} = e^4 \left\{ \exp \left[- \left(\frac{x + x_{\text{ini}}}{b} \right)^2 \right] \pm \exp \left[- \left(\frac{x - x_{\text{ini}}}{b} \right)^2 \right] \right\} e_x, \quad (20)$$

where $x_{\text{ini}} = X_R + a_x + 2b$, and we recall that $[X_R = d/2, b = \min(a_x, a_y)]$. The coefficient e^4 is introduced only for plotting purposes, the magnitude being immaterial for linear studies. Equation (20) represents a pair of planar compressible perturbations concentrated in the ambient corona, exciting S_x (A_x) motions when the plus (minus) sign applies.

2.4. Parameter Overview and Solution Method

The behavior of small-amplitude perturbations is determined by two sets of parameters. We take the dimensional set to be $\{\rho_e, b, v_{\text{Ae}}\}$, which serves merely as normalizing constants in our context. Accept that we are primarily interested in such timescales as the oscillation period and some damping time. The importance of the dimensionless set then follows from a straightforward dimensional analysis, which dictates that a timescale t_{scale} is formally expressible as

$$\frac{v_{\text{Ae}} t_{\text{scale}}}{b} = \mathcal{F} \left[\text{orientation}, \frac{\rho_i}{\rho_e}, \frac{a}{b}, \bar{l}, \frac{d}{b}; \quad kb; \quad \text{perturbation pattern} \right]. \quad (21)$$

The subgrouped parameters characterize the transverse structuring, axial wavenumber, and initial perturbation, respectively. By “orientation” we refer to either “ x -major” or “ x -minor”. By “perturbation pattern” we mean either S_x or A_x . We fix the axial wavenumber at $kb = \pi/30$ throughout, meaning a tube length $L = 30b$ for axial fundamentals. This L/b suffices for our purposes, lying toward the lower end of but within the accepted range for AR loops imaged in the EUV (e.g., Aschwanden et al. 2004; Schrijver 2007). Table 1 briefly overviews our computations, which are grouped into four sets to be detailed later. The density contrast ρ_i/ρ_e is fixed at either 3 or 5, both values being representative of AR loops (e.g., Aschwanden et al. 2004, and references therein).

We solve Eqs. (7) to (11) with the following procedure. A computational domain $[-x_M, x_M] \times [-y_M, y_M]$ is discretized into a uniform mesh with identical spacing in the x - and y -directions ($\Delta_x = \Delta_y = \Delta$). The zero-gradient condition is implemented for all unknowns at all boundaries. We evolve Eqs. (7) to (11) with the classic MacCormack scheme (MacCormack 1969), a popular finite-difference algorithm second-order accurate in both space and time (see the textbooks by, e.g., Anderson 1995; Jardin 2010, for more). The time step Δ_t is set via some effective Courant number $c := (v_{\text{Ae}} \Delta_t / \Delta_x)^{2/3} + (v_{\text{Ae}} \Delta_t / \Delta_y)^{2/3}$ as inspired by Hong (1996). A value of $c = 0.99$ is employed for all the presented results. We have verified that varying c between ~ 0.7 and ~ 1.3 introduces no discernible difference, and numerical stability is consistently maintained.

Some remarks on the grid setup are necessary. We start by noting that the spatial spacing Δ restricts the timeframe in which numerical solutions make physical sense, an aspect raised by Terradas et al. (2008b, hereafter T08) who numerically solved an equivalent set of governing equations. Defining the Alfvén frequency $\omega_A(x, y) = kv_A(x, y)$, one expects that some time-dependent phase-mixing length will emerge as (Mann et al. 1995)

$$L_{\text{ph}}(x, y; t) = \frac{2\pi}{|\nabla \omega_A(x, y)|t}, \quad (22)$$

which characterizes the transverse lengthscales of resonantly generated Alfvénic motions in the nonuniform portions in the system. It suffices to consider only the nonuniform layer of one tube. Evidently, the shortest phase-mixing length $L_{\text{ph}}^{\text{min}}(t)$ at a given instant occurs at the strongest $|\nabla \omega_A(x, y)|$. Equally evident is that this strongest $|\nabla \omega_A(x, y)|$ depends only on ρ_i/ρ_e and \bar{l} even when elliptic tubes are examined. Let $L_{\text{ph}}^{\text{min}}(500)$ denote $L_{\text{ph}}^{\text{min}}$ at $t = 500b/v_{\text{Ae}}$, before which our computations are consistently terminated. It then follows from the arguments by T08 that our signals are physically relevant provided $L_{\text{ph}}^{\text{min}}(500) \geq 2\Delta$. As shown by Table 1, this criterion is satisfied by the reference grid setup for any set of our computations.

Table 1. Summary of time-dependent solutions presented in the text

Set	ρ_i/ρ_e	\bar{l}	$L_{\text{ph}}^{\text{min}}(500)$	Reference Grid	Section	Remarks
1	3	≥ 0.2	$\gtrsim 0.032b$	$[x_M, y_M] = [12b, 12b], \Delta = 0.01b$	§3.1	1-circular-tube
2	5	$\gtrsim 0.182$	$\gtrsim 0.019b$	$[x_M, y_M] = [12b, 10b], \Delta = 0.005b$	§3.2	2-circular-tube
3	3	0.4	0.063b	$[x_M, y_M] = [30b, 25b], \Delta = 0.01b$	§4.1	2-elliptic-tube x-major
4	3	0.4	0.063b	$[x_M, y_M] = [30b, 25b], \Delta = 0.01b$	§4.2	2-elliptic-tube x-minor

Notes. All computations pertain to $kb = \pi/30$ or equivalently $L/b = 30$ for axial fundamentals.

3. Test Computations for Circular Tubes

The MacCormack scheme, while a textbook one, has not been applied to Eqs. (7) to (11). Its applicability is therefore examined in this section via some test computations for which the time-dependent behavior can be established or expected with independent methods. Only circular tubes are of interest, and we refer to $b(= a)$ as our tube radius. We start by examining the response of a one-circular-tube system to axisymmetric (sausage) perturbations, following our previous study (Li et al. 2022) to formulate both the equilibrium and the initial perturbation. The Fourier-integral-based solutions, presented in Fig. 4 therein, agree closely with our MacCormack solutions. In particular, no discernible numerical anisotropy shows up even though finite differences are performed on a Cartesian grid to examine a non-planar equilibrium (see e.g., the review by Sescu 2015, for more on numerical anisotropy). The rest of this section focuses on kink perturbations.

3.1. Kink Motions in a One-Circular-Tube Setup

This subsection examines kink perturbations in a one-circular-tube configuration, placing the tube center at the origin without loss of generality. The equilibrium density is realized through Eqs. (16) and (17) by taking $[a_x = a_y = b, X_j = 0]$ and then dropping the subscript j . Kink motions in such a configuration have been extensively studied (see the review by Nakariakov et al. 2021, and references therein), readily allowing our MacCormack computations to be compared with known results. By “known” we refer to two sets of studies. Set one, presented in Sect. 4 of T08, adopts the RR02 implementation to examine the system response to an initial perturbation of the form

$$v_{\text{ini}}(x, y) = v_{\text{Ae}} \exp \left[-\frac{(y - y_{\text{ini}})^2}{\sigma^2} \right] \mathbf{e}_y. \quad (23)$$

Figure 2 in T08 then presents the time sequence of v_y sampled at the tube center for a combination of parameters $[\rho_i/\rho_e = 3, kR = \pi/20, \ell/R = 0.6]$ and $[y_{\text{ini}} = 3R, \sigma = R]$. We repeat the same experiment, using Eq. (19) to address notational differences and adopting an identical computational grid. Our finite-difference results are found to be consistent with T08, despite that the numerical code therein adopts the finite-volume methodology.

We proceed to perform an additional series of computations to examine whether our code outputs agree with expectations for ideal kink quasi-modes. Let $\omega = \Omega - i\gamma$ denote the complex-valued quasi-mode frequency, and see Ω and γ as positive. With the kink speed c_{kink} defined as

$$c_{\text{kink}}^2 := \frac{\rho_i v_{\text{Ai}}^2 + \rho_e v_{\text{Ae}}^2}{\rho_i + \rho_e}, \quad (24)$$

it is well established that (RR02; see also Goossens et al. 1992 and Soler et al. 2013)

$$\Omega \approx kc_{\text{kink}},$$

$$\frac{\gamma}{\Omega} \approx \frac{1}{4} \frac{\bar{l}}{1 - \bar{l}/2} \frac{\rho_i/\rho_e - 1}{\rho_i/\rho_e + 1} \quad (25)$$

in the so-named thin-tube-thin-boundary limit (TTTB, $kb \ll 1$ and $\bar{l} \ll 1$). Note that the TTTB expressions are usually formulated in terms of the RR02 notations $[R, \ell]$. Note also that the TTTB results may not hold well beyond their range of applicability (e.g., Soler et al. 2014; Yu et al. 2021). We therefore also evaluate the mode frequencies numerically with the general-purpose finite-element code PDE2D (Sewell 1988), computing ideal kink quasi-modes as resistive eigenmodes (see Goossens et al. 2011 for conceptual clarifications; see also Terradas et al. 2005 for the first introduction of PDE2D to solar contexts)¹. No restriction is necessary for kb or \bar{l} .

¹ A uniform resistivity η is employed for simplicity, the associated magnetic Reynolds number $R_m := \mu_0 R v_{\text{Ai}}/\eta = 10^5$. We have verified that further increasing R_m does not introduce any discernible difference to the oscillation frequencies and damping rates. These η -independent values are well known to be physically connected to ideal quasi-modes (e.g., Poedts & Kerner 1991; Terradas et al. 2006; Soler et al. 2013).

The rest of this subsection is devoted to a fixed combination $[\rho_i/\rho_e = 3, kb = \pi/30]$, allowing only \bar{l} to vary. Furthermore, the reference grid (see Table 1) is consistently employed in our time-dependent computations, where kink motions are excited by a perturbation of the fixed form

$$\frac{v_{\text{ini}}(x, y)}{v_{\text{Ae}}} = e^4 \exp \left[-\frac{(x + 3b)^2}{b^2} \right] e_x. \quad (26)$$

Equation (26) is essentially identical to Eq. (23) except that v_x rather than v_y is perturbed. Figure 2a examines a representative case with $\bar{l} = 0.4$, showing the temporal evolution of the x -speed sampled at the tube center ($v_x(0, 0, t)$, the solid curve). This v_x signal is seen to feature some rapid variations for $t \lesssim 15b/v_{\text{Ae}}$. By “rapid” we mean timescales on the order of the transverse Alfvén time (b/v_{Ai}), which derives from the multiple reflections off the tube boundaries that are imparted by the external driver to the tube. The v_x signal transitions toward a regular slower-varying pattern afterwards, becoming monochromatic when $t \gtrsim 70b/v_{\text{Ae}}$. We choose to leave out the first extremum in this stage for safety, and fit the segment encompassing the next six (the red asterisks) with an exponentially damped cosine

$$f_{\text{fit}}(t) \propto \exp \left(-\frac{t}{\tau} \right) \cos \left(\frac{2\pi t}{P} + \phi \right). \quad (27)$$

The damping envelope from the best-fit is then plotted for the entire duration in Fig. 2a by the dashed curves. One sees that this best-fit envelope, while deduced for some segment, offers a good description for the larger-time behavior as well (say, $t \gtrsim 300b/v_{\text{Ae}}$).

Figure 2b surveys a range of \bar{l} by plotting the oscillation frequencies (Ω_{fit} , the black open circles) and damping rates (γ_{fit} , blue), which are translated from the best-fit periods and damping times ($\Omega_{\text{fit}} = 2\pi/P_{\text{fit}}$ and $\gamma_{\text{fit}} = 1/\tau_{\text{fit}}$). Note that Ω is measured in units of the external Alfvén frequency $\omega_{\text{Ae}} = kv_{\text{Ae}}$, and γ/Ω is presented rather than γ itself. The curves in Fig. 2b further provide the quasi-mode expectations with either the analytical TTTB expression (Eq. 25, the solid lines) or the PDE2D computations (labeled “Resistive”, dashed). One sees that the TTTB results provide a rather good approximation to the numerical “Resistive” ones, the frequencies being practically the same and the damping rates differing by $\gtrsim 10\%$ only when $\bar{l} \gtrsim 0.4$. One further sees that the open circles agree well with the “Resistive” computations, demonstrating that the internal flow fields practically evolve as an ideal quasi-mode at least in the interval where the fitting is performed.

3.2. Kink Motions in a Two-Circular-Tube Setup

This subsection examines kink motions in a two-circular-tube configuration, for which the distinction between S_x and A_x patterns becomes necessary. The initial perturbation is therefore chosen to follow Eq. (20), where x_{ini} evaluates to $d/2 + 3b$. Our code consistently adopts the $[b, \bar{l}]$ notations. However, the mixed usage of the RR02 convention $[\mathcal{R}, \ell]$ turns out to be necessary. The reason is that this RR02 convention was adopted by SL15 to examine ideal quasi-modes from an eigenvalue-problem perspective in a configuration physically identical to ours. Briefly put, the study by SL15 is based on the TB-embedded T-matrix formalism of scattering theory, the pertinent results being most straightforward for our time-dependent computations to be compared with. By “pertinent” we specifically refer to Fig. 4 therein, which presents the ℓ/\mathcal{R} -dependencies of the quasi-mode frequencies and damping rates for a fixed combination $[\rho_i/\rho_e = 5, d/\mathcal{R} = 2.5, k\mathcal{R} = \pi/100]$. Note that varying ℓ/\mathcal{R} actually impacts our \bar{l} , d/b , and kb simultaneously (see Eq. 19). We adopt a fixed $kb = \pi/30$ to save computational time. This does not matter because we will measure our timescales or frequencies in appropriate units (say, Ω in ω_{Ae}) and the resulting readings do not depend on $k\mathcal{R}$ when $k\mathcal{R} \lesssim \pi/20$ (see Fig. 3 in SL15, and note that $k\mathcal{R} < kb$). Equation (19) readily converts the pair $[\ell/\mathcal{R}, d/\mathcal{R}]$ into our $[\bar{l}, d/b]$.

We now test our time-dependent computations against the SL15 results, to be labeled “T-matrix” for clarity. It suffices to examine the time sequences of the x -speed sampled at the left tube center (namely, $v_x(-d/2, 0; t)$); the right counterpart is either identical (for S_x) or different only by sign (for A_x). Figure 3 focuses on the choice $\ell/\mathcal{R} = 0.4$, and plots the sampled v_x for (a) the S_x and (b) the A_x patterns by the solid curves. The same analysis as in Fig. 2a is then repeated for both curves, whereby we single out the six extrema (the red asterisks in Fig. 3) after the transitory phase to perform a fitting with Eq. (27). The best-fit exponential envelope, plotted by the dashed curves for the entire duration, is seen to well reflect the damping of kink motions for much longer time.

Figure 4 proceeds to examine the ℓ/\mathcal{R} -dependencies of (a) the oscillation frequencies (Ω in ω_{Ae}) and (b) damping-rate-to-frequency ratios (γ/Ω). The S_x and A_x patterns are discriminated by the different colors. We present the best-fit values from our time-dependent computations by the open circles, and overplot the T-matrix results by the solid curves for comparison. Note that these T-matrix curves are read from Fig. 4 of SL15. Our best-fit results are seen to compare favorably with the T-matrix results, which is particularly true when $\ell/\mathcal{R} \lesssim 0.3$. This statement holds despite the somewhat visible difference in Ω at, say, $\ell/\mathcal{R} = 0.2$, where the best-fit value actually deviates from its T-matrix counterpart by only $\sim 2.7\%$. One further sees that the most significant departure occurs for the A_x damping rate when $\ell/\mathcal{R} = 0.4$. However, this difference is rather modest and reads $\sim 21.7\%$ in relative terms. We therefore conclude that the dispersive properties of kink quasi-modes can be reasonably computed by incorporating the shortcut TB formulae in the T-matrix framework for all ℓ/\mathcal{R} examined here². Our time-dependent results, on the other hand, further corroborate the SL15 conclusion that A_x motions possess higher frequencies and damp more rapidly than S_x ones.

² Some discrepancy exists in the literature regarding the damping of lower-order kink motions when the tubes are in contact. The T-matrix results by SL15 indicate that these motions remain damped (see Fig. 2 therein), whereas damping was found to disappear in the modal studies formulated in bi-cylindrical coordinates (Robertson & Ruderman 2011; Gijzen & Van Doorslaere 2014). Our IVP study supports the SL15 conclusion. The use of a bi-cylindrical coordinate system was recognized by the referenced studies to be physically problematic for small tube separations.

3.3. Interim Summary on Numerical Aspects

This subsection further justifies our numerical treatment. An additional series of computations have been performed to address the effects of the grid spacing Δ and the domain size $[x_M, y_M]$. These results are collected in Appendix A to streamline the main text. Overall, we have verified that the MacCormack scheme is appropriate for our purposes, with no issue arising from the application to nonplanar structures of the finite-difference methodology on a Cartesian grid. The zero-gradient boundary condition is somehow not fully transparent to perturbations excited by our planar drivers, and the domain size somehow impacts how the internal flows transition to a quasi-mode behavior. However, this domain size effect is practically negligible on the best-fit periods (P_{fit}) and damping times (τ_{fit}) that we derive for the quasi-mode stage. Likewise, the computed internal flows are not affected by the grid spacing Δ provided that Δ is sufficiently small.

4. Kink Motions in a Two-Elliptic-Tube Setup

This section is devoted to kink motions in a two-elliptic-tube configuration, for which the x -major and x -minor orientations need to be discriminated. The reference grid ($[x_M = 30b, y_M = 25b, \Delta = 0.01b]$, see Table 1) will be consistently adopted, enabling a meaningful comparison between the tube orientations. The notations $[a, b, \bar{l}]$ are adopted throughout this section, where all computations pertain to a fixed combination of physical parameters $[\rho_i/\rho_e = 3, \bar{l} = 0.4, kb = \pi/30]$. We adjust only the dimensionless tube separation (d/b) and the ratio of the semi-major to semi-minor axis (a/b) for a given orientation and a given perturbation pattern (see Eq. 21). Tube overlapping is always avoided. The equilibria are consistently perturbed with Eq. (20).

4.1. S_x and A_x Motions for the x -major Orientation

This subsection addresses the x -major orientation. We start with Fig. 5 to present the temporal evolution of the x -speed sampled at the left tube center ($v_x(-d/2, 0; t)$, the solid lines) for both (a) the S_x and (b) the A_x motions. The tube separation is fixed at $d = 5b$, whereas a number of values are examined for a/b as discriminated by the different colors. Only the variations after the rapid-varying phase are of interest for any v_x sequence. We somehow emphasize the segment exactly encompassing the six extrema starting with the one labeled by the relevant asterisk, performing a fitting procedure with Eq. (27). A best-fit exponential envelope results, with an example plotted over the entire duration for the case where $a/b = 2.5$. With this example we demonstrate that an exponentially damped cosine is in general adequate for describing the v_x sequences after the rapid-varying phase. The best-fit periods and damping times thus derived will be understood as pertaining to an ideal quasi-mode.

The temporal attenuation of the internal flow fields means energy redistribution in ideal MHD. Let us take the case with $a/b = 2.5$ in Fig. 5, and note that the two tubes are actually in contact ($d = 5b = 2a$). Figure 6 presents the spatial distribution of the velocity fields ($\mathbf{v} = v_x \mathbf{e}_x + v_y \mathbf{e}_y$, the blue arrows) and the instantaneous energy density (ϵ , filled contours) for (a) the S_x and (b) A_x motions at an arbitrarily chosen instant $t = 260b/v_{Ae}$. A subarea of the second quadrant is singled out by each inset to emphasize the ϵ distributions in the nonuniform layers of both tubes, with the red curves delineating the layer boundaries. The white curve further indicates where the local Alfvén frequency equals the quasi-mode frequency. Figure 6 is actually taken from the attached animation. The arrows and filled contours are plotted in a way that it makes sense to compare the \mathbf{v} or ϵ strengths not only in one snapshot but between different instants for a given orientation. In particular, the darker a portion is, the larger the value of ϵ therein.

Consider first the ambient fields for both perturbation patterns, where by “ambient” we refer to the flows some distance away from the tubes. Likewise, by “tube flow” we mean the field excluding the ambient flow, and by “internal flow” we refer specifically to the uniform portion inside either tube. For both patterns, one sees from the animation that the ambient flows tend to vary more rapidly than the internal ones. This feature is particularly clear for the S_x pattern because the ambient flows tend to be substantially stronger than the internal flows as well. Regardless, a periodogram analysis yields that the ambient flows follow primarily the external Alfvén frequency ω_{Ae} , whereas the variations of the internal flows are by far dominated by the lower quasi-mode frequency. That the ambient motions are not coordinated with the internal ones is a result of the form of the initial exciter given by Eq. (20). The relevant physics is actually very similar to what happens in the T08 study despite the configurational differences, the key being the y -invariance of Eq. (20). It proves easier to explain this by considering a uniform equilibrium with density ρ_e , for which Eqs. (7) to (11) can be combined to yield a Klein-Gordon equation if the y -dependence is dropped (see Eq. 1 in Terradas et al. 2005). Suppose that an individual component in Eq. (20) is applied. A dispersive fast wave then results, whereby any fluid parcel in the system eventually ends up in some oscillatory wake at the Alfvén frequency ω_{Ae} (see Fig. 1 in Terradas et al. 2005). Oscillatory wakes turn out to still exist in the ambient flow when the two elliptic tubes are introduced, and when an additional planar perturbation is implemented. Note that the initial perturbations are external to our tubes. Note further that overall the large-time behavior for the ambient flow actually comprises two component wakes, each being the response to the corresponding component driver. The two component wakes tend to interfere constructively (largely destructively) for the S_x (A_x) pattern, thereby explaining the strength of the ambient flow relative to the internal one.

Now examine the tube flows. Focusing on the blue arrows, one sees from Fig. 6 that the gross patterns for both S_x and A_x are similar to Fig. 2 in L08 despite that a two-circular-tube equilibrium with piece-wise constant profile was addressed therein. Specifically, the internal velocity field is more or less uniform, and a pair of vortical motions develop at the edge of either tube. These two features, combined with the overall symmetric properties of the internal field about $x = 0$, demonstrate the robustness of the classification scheme for lower-order kink motions. The primary difference from L08, on the other hand, is that the vortical motions gradually evolve from a simple dipolar behavior (see the first several instants in the animation) into multiple shearing layers (Fig. 6). This evolution is well known for kink motions in isolated tubes with either circular (e.g., Terradas et al. 2008a; Pascoe et al. 2010; Antolin et al. 2014) or elliptic cross-sections (e.g., Ruderman 2003; Guo et al. 2020). What Fig. 6 demonstrates is then that tube interactions do not compromise the phase-mixing physics behind this evolution. That said, tube interactions do

impact the detailed development of the small-scale shears, as evidenced by the differences in the velocity fields for the two different perturbation patterns. Suppose that tube interactions are negligible. The tube flows are then expected to be identical for the S_x and A_x patterns, meaning in particular a symmetric distribution of the energy density (ϵ) with respect to the minor axis ($x = -d/2 = -2.5b$ here). However, this expectation roughly holds only for the S_x pattern (Fig. 6a inset), whereas the left portion in the left tube is favored in the ϵ distribution for the A_x pattern (Fig. 6b inset). Besides phase-mixing, a closely related aspect that is not fundamentally compromised by tube interactions is the resonant interplay between the quasi-mode and the Alfvén continuum (see Soler & Terradas 2015 and references therein for the subtle distinction between resonant absorption and phase-mixing). By this we refer to two features common to the S_x and A_x patterns, and we concentrate on the insets in the animation. Firstly, the attenuation of the internal field is accompanied by the accumulation of perturbation energies in the nonuniform layer. Secondly, this energy accumulation leads to a localized ϵ distribution, with the strongest perturbations tending to the white resonance contour as time proceeds for roughly one quasi-mode period after the rapid-varying phase. Overall with Fig. 6 we conclude that the notions of phase-mixing and resonant absorption remain applicable to kink motions in our two-elliptic-tube configuration.

Figure 7 further examines the phase-mixing process by showing the y -cuts of the x -speeds through the left tube center for both (a) the S_x and (b) the A_x patterns. A number of instants are rather arbitrarily chosen and discriminated by the different colors. The vertical dotted lines mark the borders of the nonuniform layer, where shearing motions ($\partial v_x / \partial y$ here) with increasingly small scales are seen to develop as time proceeds. We choose to quantify this development by relating the number of the v_x extrema ($N_{\text{extm}}(t)$) to the instantaneous phase variation accumulated over the Alfvén continuum ($\phi_{\text{ac}}(t)$, see the discussion on Eq. A.1). Note that $\phi_{\text{ac}}(t) = (\omega_{\text{Ae}} - \omega_{\text{Ai}})t$ is identical for both perturbation patterns, corresponding specifically to $[2.82, 4.23, 5.64]$ half-cycles for the examined instants. One then expects $[2_{+0}^{+1}, 4_{+0}^{+1}, 5_{+0}^{+1}]$ extrema in the v_x profiles in Figs. 7a and 7b, which is indeed the case³. As can be readily verified, that $N_{\text{extm}}(t) = \lfloor \phi_{\text{ac}}(t) / \pi \rfloor$ at these instants actually constrains the phase φ_0 in Eq. (A.1) to a very narrow range $[q\pi, (q + 0.19)\pi]$ with $q = 0, 1$.

Figure 8 proceeds to examine (a) the periods P and (b) damping-time-to-period ratios τ/P of kink quasi-modes pertaining to both the S_x (the solid curves) and the A_x (dashed) patterns, showing how P and τ depend on the ratio of the semi-major to semi-minor radius (a/b) for a given tube separation (d). We also examine a number of d as discriminated by the different colors. Note that this survey adopts a fixed combination of physical parameters [$\rho_i/\rho_e = 3, \bar{l} = 0.4, kb = \pi/30$]. The same set of parameters is additionally adopted to evaluate P and τ/P of the kink quasi-mode for an isolated circular tube with the resistive eigenmode approach (see Sect. 3.1), the results being plotted by the horizontal lines for comparison. Note that the values for P (in units of the axial Alfvén time $T_{\text{axial}} = 2\pi/\omega_{\text{Ae}} = 2L/v_{\text{Ae}}$) and τ/P vary little if $kb = \pi b/L$ is further reduced, meaning that little will change if one examines axial fundamentals in AR loops with much larger L/b than adopted here. Note further that a/b is required not to exceed $d/2b$ for a given d/b such that tube overlapping is avoided. For any given pair $[a/b, d/b]$, Fig. 8 indicates that the A_x motion possesses a shorter period and damps more efficiently than the S_x motion. This behavior is identical to what SL15 found for two-circular-tube configurations. The argument therein is that A_x motions are more “forced”; the two tubes move largely in a synchronous fashion for the S_x pattern, whereas the flows in between the two tubes periodically “collide” when the A_x pattern is examined. The same argument applies here although elliptic tubes are addressed, with the insets of Fig. 6b already hinting at a more forced behavior for A_x motions. Also similar to SL15 is that, for a given a/b , the difference between the values of P (or τ/P) for the S_x and A_x motions tends to decrease monotonically with d . This agrees with the intuitive expectation for a weaker tube interaction.

Let us pay more attention to the overall behavior for P to increase monotonically with a/b for a given d/b . Somehow subtle is that tube interactions also have some effect, because increasing a/b actually brings the two tubes effectively closer even if the distance between the tube centers is fixed. Regardless, this tube interaction only plays a minor role, given that the monotonical a/b -dependence takes place for different d and for the S_x and A_x motions alike. One may therefore expect the same a/b -dependence for isolated elliptic tubes (or equivalently $d/b \rightarrow \infty$), in which case it is no longer necessary to distinguish between the S_x and A_x patterns. This was indeed seen in our previous IVP study (Guo et al. 2020), where we offered some heuristic argument similar to the earlier one by Ruderman (2003). For simplicity, suppose that the equilibrium configuration is transversely structured in a piece-wise constant manner. The heuristic argument then relies on the observation that the velocity normal to the tube edge plays a central role for an isolated density-enhanced tube to communicate with its surroundings. Evidently, a larger a/b makes the tube edge more elongated in the x -direction. Their velocities primarily x -directed, the fluid parcels in the tube interior therefore become less aware of the surroundings, meaning some enhanced effective inertia and hence a longer period. The same argument can be invoked in this study, despite the subtlety that the fluids surrounding one tube actually embed another tube.

4.2. S_x and A_x Motions for the x -minor Orientation

This subsection addresses the x -minor orientation. We start with Fig. 9 where the same set of physical quantities as in Fig. 5 is employed, and the time sequences for the x -speed sampled at the left tube center are presented in an identical format. A fitting procedure is once again performed for any v_x sequence over the duration exactly enclosing the six extrema starting with the one indicated by the pertinent asterisk. We take the view that the best-fit periods (P) and damping times (τ) pertain to the ideal quasi-modes supported by our two-elliptic-tube configuration.

Figure 10 specializes to the case with $[a/b = 2.5, d/b = 5]$, following the same format as in Fig. 6 to present the velocity fields (the blue arrows) and the spatial distributions of the perturbation energy density (ϵ , filled contours) at a representative instant. Note

³ The velocity shears are prone to the Kelvin-Helmholtz instability (KHi), as was first theoretically recognized in the wave context by Heyvaerts & Priest (1983) and Browning & Priest (1984). Further nonlinear simulations have demonstrated that the KHi may arise in the early stage of the evolution of kink motions for isolated tubes (e.g., Terradas et al. 2008a; Antolin et al. 2015; Shi et al. 2021) and multi-tube setups alike (e.g., Magyar & Van Doorselaere 2016; Guo et al. 2019a). The applicability of such linear results as presented here may therefore need to be assessed on a case-by-case basis when real data are analyzed (see Sect. 10 of the review by Nakariakov et al. 2021, for more on the nonlinear aspects).

that the tubes are quite some distance apart in this case. Note also that Fig. 10 is a snapshot extracted from the attached animation. Focusing on the velocity fields, one can safely conclude from the animation that the notations of S_x and A_x make physical sense as proposed by L08 for two-circular-tube systems. For both perturbation patterns, the insets in the animation further indicate that the attenuation of the internal flows is accompanied by the enhancement of perturbation energy density ϵ in the nonuniform layers, with the localization of ϵ strongly mediated by the Alfvén resonance. This latter point can be readily drawn from the close association of the darkest portion in either ϵ distribution with the white curve marking where the quasi-mode frequency matches the local Alfvén frequency.

Figure 11 presents, in a format identical to Fig. 7, the y -cuts of the x -speed through the left tube center for a number of arbitrarily chosen instants. The aim is also to show the key role that phase-mixing plays for the gradual development of shearing motions with increasingly small scales in the nonuniform layers. We follow Fig. 7 to quantify this with the aid of Eq. (A.1), once again counting the instantaneous number $N_{\text{extm}}(t)$ of the v_x extrema. The pertinent instantaneous phase variations ($\phi_{\text{ac}}(t)$), on the other hand, are the same as in Fig. 7 and read $[2.82, 4.23, 5.64]\pi$ for the examined instants. However, somehow different is that the relevant values for N_{extm} now may deviate from $[\phi_{\text{ac}}/\pi]$, attaining specifically $[3, 4, 5]$. This deviation is readily attributable to the phase φ_0 in Eq. (A.1). Conversely, this set of deviations can be readily verified to constrain φ_0 to a rather narrow range of $[(q + 0.19)\pi, (q + 0.37)\pi]$ with $q = 0, 1$.

Figure 12 moves on to survey (a) the quasi-mode periods P and (b) damping-time-to-period ratios τ/P for a substantial range of combinations $[a/b, d/b]$. This figure is identical in format to Fig. 8. The values examined for the tube separation d consistently avoid tube overlapping, and hence there is no need to constrain the ratio of the semi-major to semi-minor axis (a/b) for a given d/b . Examine Fig. 12a first, from which one sees the expected monotonic behavior for the differences between the S_x and A_x periods to decrease with d/b for a given a/b . For a given separation d/b , one further sees that the values of P tend to decrease monotonically with a/b for the S_x and A_x motions alike. However, tube interactions remain possible to be partly responsible for this a/b -dependence, because the area between the two tubes actually broadens with a/b even if d/b is fixed. This tube-interaction effect can hardly be dismissed given that the S_x and A_x values deviate more strongly when a/b increases for a given d/b . Having said that, it remains possible to partly explain the monotonic a/b -dependence of P by invoking the inertia arguments initially offered for isolated density-enhanced elliptic tubes. Note that the tube edges are now more elongated in the y -direction, whereas the fluids parcels in either tube interior remain to oscillate primarily in the x -direction. It therefore holds that an increase in a/b makes the internal fluid parcels better aware of the external medium, meaning some reduced effective inertia and hence a shorter period.

Consider now Fig. 12b where the damping-time-to-period ratios (τ/P) are examined. Two features arise when $a/b \lesssim 1.5$, one being that A_x motions attenuate more efficiently than S_x ones, the other being that the differences between the S_x and A_x values tend to decrease with tube separation. These features resemble what happens for two-circular-tube systems, and are expected because the cross-sectional shapes are not far from circular. However, the behavior of τ/P at larger a/b is considerably more complicated than in Fig. 8b where the x -major orientation is addressed. By “complicated” we specifically refer to the nonmonotonic d/b -dependence of τ/P for either perturbation pattern. Take the case with $a/b = 2.5$. When d/b increases, one sees an increase followed by some decrease in τ/P for the S_x motion, whereas τ/P tends to decrease for the A_x motion. This latter simplicity is only apparent, because τ/P is bound to increase with d/b again such that the A_x values eventually join their S_x counterparts when the tubes are sufficiently separated. We have verified that the somehow involved behavior of τ/P is not of numerical origin (see Sect. 3). Furthermore, it matters little as to how to choose the segment of a v_x sequence for fitting, provided that this segment starts sufficiently later than the rapid-varying phase (see Fig. 9). The most likely reason is then that the perturbations in between the two tubes depend on a/b and d/b in an intricate fashion, and hence an intricate dependence on a/b and d/b of the efficiency of tube interactions. Regardless, the reason behind the d/b -dependence of τ/P is also behind, say, the nonmonotonic a/b -dependence of τ/P for A_x motions for a given d/b (see the dashed curves), and the occasional behavior for S_x motions to damp more efficiently (compare the black solid and dashed curves).

5. Implications for Coronal Seismology

This section discusses some seismological implications of our study. Only axial fundamentals are considered. We restrict ourselves to the inference of the axial Alfvén time ($T_{\text{axial}} = 2L/v_{\text{Ae}}$) and the dimensionless nonuniform layer width (\bar{l}). We further assume that neighboring elliptic tubes are imaged in, say, the EUV when the line of sight lies in the tube plane (see Fig. 1a), meaning that the tubes may be readily mistaken as circular ones.

Let us start with Figure 8 where our x -major computations are summarized, and consider only the S_x motion for $[a/b = 2.5, d/b = 5]$. Now assume that the relevant oscillating tubes possess the “true” dimensionless values $[\rho_i/\rho_e = 3, \bar{l} = 0.4]$ (note that L/b is immaterial when sufficiently large). Let P_{obs} and $(\tau/P)_{\text{obs}}$ be the measured values of the period and damping-time-to-period ratio, and we take $(\tau/P)_{\text{obs}} = 6.39$ to comply with Fig. 8. One therefore deduces a “true” value of $P_{\text{obs}}/1.6$ for T_{axial} , which is recalled to be dimensional. Now suppose that the density contrast is measured to be $\rho_i/\rho_e = 3$, and let us follow the customary practice to infer T_{axial} and \bar{l} by seeing the S_x motion as a kink quasi-mode in an isolated circular tube. It matters little regarding whether one assigns a or b to the tube radius. The dimensionless quasi-mode period P/T_{axial} depends essentially only on ρ_i/ρ_e , always attaining ~ 1.42 when $\bar{l} \lesssim 0.6$ (see the green horizontal line in Fig. 8a; see also Fig. 2b). One therefore deduces a value of $P_{\text{obs}}/1.42$ for T_{axial} , which differs from the true value by $\sim 13\%$. However, it is considerably more problematic when $(\tau/P)_{\text{obs}}$ is invoked to infer \bar{l} . Employing the resistive eigenmode approach, we find that a $(\tau/P)_{\text{obs}} = 6.39$ results in a $\bar{l} \approx 0.18$, which underestimates the true value by $\sim 55\%$. One may argue that this difference is not that significant; after all the customary seismological practice yields the correct qualitative picture that the oscillating tube possesses a thin boundary. Our point, however, is that care needs to be exercised when $(\tau/P)_{\text{obs}}$ is put to quantitative use, with the uncertainties in the deduced dimensionless layer width \bar{l} readily exceeding $\sim 50\%$ if one neglects the combined effect of tube cross-sectional shapes and tube interactions.

Now move on to Fig. 12 where our x -minor computations are summarized. We assess what uncertainties the customary practice may introduce to the axial Alfvén time $T_{\text{axial}} = 2L/v_{\text{Ae}}$ and dimensionless layer width \bar{l} by neglecting the joint effects of cross-sectional shapes and tube interactions. The procedure is identical to what we performed for the x -major orientation; we accordingly choose the A_x values for $[a/b = 2.5, d/b = 3]$ given that they deviate the most from the horizontal lines. Consider the period first. One infers a true value of $T_{\text{axial}} = P_{\text{obs}}/1.13$ with Fig. 12a, whereas the customary practice remains to yield a $T_{\text{axial}} \approx P_{\text{obs}}/1.42$ or equivalently some underestimation by $\sim 20\%$. This uncertainty in T_{axial} is larger than for the x -major orientation. Now taking $(\tau/P)_{\text{obs}} = 3.44$ from Fig. 12b as measured, one deduces with the customary practice a dimensionless layer width of $\bar{l} = 0.25$ or some underestimation of the true value ($\bar{l} = 0.4$) by $\sim 38\%$. Somehow smaller than for the x -major case, this uncertainty remains substantial enough to corroborate our claim that the inhomogeneity scales deduced with the customary practice need to be treated with caution.

6. Summary

With coordinated transverse displacements in neighboring active region (AR) loops in mind, we have addressed damped kink motions in straight equilibria where two identical parallel density-enhanced tubes with elliptic cross-sections (elliptic tubes) are embedded in an ambient corona. Linear, ideal, pressureless MHD was adopted throughout. We concentrated on axially standing motions, formulating the ensuing two-dimensional (2D) initial value problem (IVP) in the plane transverse to the equilibrium magnetic field. We identified the direction connecting the tube centers as horizontal, discriminating two tube orientations where either the major (dubbed “ x -major”) or the minor (“ x -minor”) axis is horizontally placed. The system evolution was initiated with external velocity drivers, implemented in such a way that the internal flow fields are primarily horizontal and are either symmetric (S_x) or anti-symmetric (A_x) with respect to the vertical axis about which our equilibrium configuration is symmetric. The temporal evolution of the velocity perturbations at tube centers was of particular interest, allowing us to identify the quasi-mode stage as where the monochromatic time sequence follows an exponentially damped envelope. We paid special attention to how the quasi-mode periods and damping times depend on the tube separation and the cross-sectional aspect ratio, thereby addressing the impact on the dispersive properties of damped kink motions from the joint effects of tube interactions and cross-sectional shapes.

Our numerical findings are summarized as follows. When two-circular-tube equilibria are examined as a special case, the quasi-mode periods and damping times found with our IVP approach are consistent with the modal analysis by Soler & Luna (2015), thereby independently justifying both the analytical T-matrix approach and the numerical results therein. We further find that the notions of resonant absorption and phase-mixing are not undermined when elliptic cross-sections are allowed for. Specifically, the nonuniform layers around tube boundaries feature both the development of velocity shears with increasingly small scales and the energy accumulation around where the local Alfvén frequency matches the quasi-mode frequency. The A_x motions are found to possess shorter periods and damp more rapidly than the S_x motions for the x -major orientation, in which case the periods and damping times for both perturbation patterns tend to increase with the major-to-minor-axis ratio. When the x -minor orientation is addressed, the A_x motions remain to oscillate more rapidly than the S_x ones. However, the periods for both patterns tend to decrease monotonically with the major-to-minor-axis ratio. Somehow subtle are the joint effects of tube interactions and cross-sectional shapes on the damping times, which may depend non-monotonically on the tube separation or the major-to-minor-axis ratio. Furthermore, the A_x motions may occasionally damp less efficiently. Neglecting these joint effects may introduce some uncertainty of $\sim 20\%$ ($\sim 50\%$) to the axial Alfvén time (the inhomogeneity lengthscale) deduced with the period (damping time). Consequently, care may need to be exercised when the damping times of kink motions are put to standard seismological practice built on wave theories for isolated circular tubes.

Some further remarks seem necessary before closing. Firstly, we note that our IVP approach is not restricted to two-tube systems but capable of handling rather generic 2D inhomogeneities. In particular, axially standing motions may be examined for straight configurations comprising multiple tubular structures with arbitrary cross-sections. Collective motions in multiple neighboring resolved loops will then be better understood, together with the motions in those apparently isolated loops that actually involve a multitude of unresolved strands (see e.g., Sect.4.2 of the review by Reale 2014 for more on this multi-stranded nature of AR loops). Secondly, that kink motions are resonantly absorbed for configurations with continuous transverse structuring is actually much-expected (e.g., the review by Goossens et al. 2011). However, somehow largely unnoticed is that the decayless regime was also observed for coordinated kink motions in adjacent AR loops (Wang et al. 2012). Accept that the transverse structuring is likely to be continuous in the relevant configurations. It then becomes necessary to address what counteracts the ensuing resonant damping, thereby bringing the understanding of decayless kink motions in multi-tube systems closer to the level of sophistication reached for the decayless regime in isolated tubes (e.g., Nakariakov et al. 2016; Guo et al. 2019b; Ruderman et al. 2021). Thirdly, coordinated motions in multiple tubular structures were identified not only in AR loops but also in, say, groups of prominence threads (see e.g., Arregui et al. 2018, for a review). To our knowledge, so far the only theoretical investigation in the prominence context was the one by Soler et al. (2009) with the T-matrix formalism. An IVP perspective is expected to be as fruitful, provided that one further account for, say, the effects associated with partial ionization (e.g., the review by Ballester et al. 2018).

Acknowledgements. This research was supported by the National Natural Science Foundation of China (41974200, 12273019, 12373055, 12203030, and 42230203). We gratefully acknowledge ISSI-BJ for supporting the international team “Magnetohydrodynamic wavetrains as a tool for probing the solar corona”, and ISSI-Bern for supporting the international team “Magnetohydrodynamic Surface Waves at Earth’s Magnetosphere and Beyond”.

References

- Aldhafeeri, A. A., Verth, G., Brevis, W., et al. 2021, *ApJ*, 912, 50
Anderson, J. D. 1995, *Computational Fluid Dynamics: the Basics with Applications* (New York: McGraw-Hill, Inc.)

- Anfinogentov, S., Nisticò, G., & Nakariakov, V. M. 2013, A&A, 560, A107
- Anfinogentov, S. A. & Nakariakov, V. M. 2019, ApJ, 884, L40
- Anfinogentov, S. A., Nakariakov, V. M., & Nisticò, G. 2015, A&A, 583, A136
- Antolin, P., Okamoto, T. J., De Pontieu, B., et al. 2015, ApJ, 809, 72
- Antolin, P., Yokoyama, T., & Van Doorselaere, T. 2014, ApJ, 787, L22
- Arregui, I. 2022, *Frontiers in Astronomy and Space Sciences*, 9, 826947
- Arregui, I. & Asensio Ramos, A. 2011, ApJ, 740, 44
- Arregui, I., Oliver, R., & Ballester, J. L. 2018, *Living Reviews in Solar Physics*, 15, 3
- Arregui, I., Soler, R., & Asensio Ramos, A. 2015, ApJ, 811, 104
- Aschwanden, M. J., Fletcher, L., Schrijver, C. J., & Alexander, D. 1999, ApJ, 520, 880
- Aschwanden, M. J., Nakariakov, V. M., & Melnikov, V. F. 2004, ApJ, 600, 458
- Aschwanden, M. J., Nightingale, R. W., Andries, J., Goossens, M., & Van Doorselaere, T. 2003, ApJ, 598, 1375
- Aschwanden, M. J. & Schrijver, C. J. 2011, ApJ, 736, 102
- Ballester, J. L., Alexeev, I., Collados, M., et al. 2018, *Space Sci. Rev.*, 214, 58
- Bogdan, T. J. & Zweibel, E. G. 1985, ApJ, 298, 867
- Bogdan, T. J. & Zweibel, E. G. 1987, ApJ, 312, 444
- Browning, P. K. & Priest, E. R. 1984, A&A, 131, 283
- Cally, P. S. 1986, *Sol. Phys.*, 103, 277
- Chen, S.-X., Li, B., Van Doorselaere, T., et al. 2021, ApJ, 908, 230
- De Moortel, I. & Nakariakov, V. M. 2012, *Philosophical Transactions of the Royal Society of London Series A*, 370, 3193
- Edwin, P. M. & Roberts, B. 1983, *Sol. Phys.*, 88, 179
- Erdélyi, R. & Morton, R. J. 2009, A&A, 494, 295
- Erdélyi, R. & Taroyan, Y. 2008, A&A, 489, L49
- Gijzen, S. E. & Van Doorselaere, T. 2014, A&A, 562, A38
- Goddard, C. R., Nisticò, G., Nakariakov, V. M., & Zimovets, I. V. 2016, A&A, 585, A137
- Goedbloed, H., Keppens, R., & Poedts, S. 2019, *Magnetohydrodynamics of Laboratory and Astrophysical Plasmas* (Cambridge University Press)
- Goossens, M., Andries, J., & Aschwanden, M. J. 2002, A&A, 394, L39
- Goossens, M., Arregui, I., Ballester, J. L., & Wang, T. J. 2008, A&A, 484, 851
- Goossens, M., Erdélyi, R., & Ruderman, M. S. 2011, *Space Sci. Rev.*, 158, 289
- Goossens, M., Hollweg, J. V., & Sakurai, T. 1992, *Sol. Phys.*, 138, 233
- Guo, M., Li, B., & Van Doorselaere, T. 2020, ApJ, 904, 116
- Guo, M., Van Doorselaere, T., Karamelas, K., & Li, B. 2019a, ApJ, 883, 20
- Guo, M., Van Doorselaere, T., Karamelas, K., et al. 2019b, ApJ, 870, 55
- Heyvaerts, J. & Priest, E. R. 1983, A&A, 117, 220
- Hong, H. 1996, *Applied Mathematics Letters*, 9, 99
- Jardin, S. 2010, *Computational Methods in Plasma Physics*, Chapman & Hall/CRC Computational Science (CRC Press)
- Keppens, R., Bogdan, T. J., & Goossens, M. 1994, ApJ, 436, 372
- Klimchuk, J. A. & DeForest, C. E. 2020, ApJ, 900, 167
- Klimchuk, J. A., Lemen, J. R., Feldman, U., Tsuneta, S., & Uchida, Y. 1992, PASJ, 44, L181
- Kucera, T. A., Young, P. R., Klimchuk, J. A., & DeForest, C. E. 2019, ApJ, 885, 7
- Li, B., Antolin, P., Guo, M. Z., et al. 2020, *Space Sci. Rev.*, 216, 136
- Li, B., Chen, S.-X., & Li, A.-L. 2022, ApJ, 928, 33
- Li, D. & Long, D. M. 2023, ApJ, 944, 8
- Lin, Y., Engvold, O. r., & Wiik, J. E. 2003, *Sol. Phys.*, 216, 109
- Luna, M., Oliver, R., Antolin, P., & Arregui, I. 2019, A&A, 629, A20
- Luna, M., Terradas, J., Oliver, R., & Ballester, J. L. 2008, ApJ, 676, 717
- Luna, M., Terradas, J., Oliver, R., & Ballester, J. L. 2009, ApJ, 692, 1582
- Luna, M., Terradas, J., Oliver, R., & Ballester, J. L. 2010, ApJ, 716, 1371
- MacCormack, R. W. 1969, AIAA Paper, 69, 354
- Magyar, N. & Van Doorselaere, T. 2016, ApJ, 823, 82
- Malanushenko, A. & Schrijver, C. J. 2013, ApJ, 775, 120
- Mann, I. R., Wright, A. N., & Cally, P. S. 1995, *J. Geophys. Res.*, 100, 19441
- McCarthy, M. I., Longcope, D. W., & Malanushenko, A. 2021, ApJ, 913, 56
- Morton, R. J. & Ruderman, M. S. 2011, A&A, 527, A53
- Nakariakov, V. M., Anfinogentov, S. A., Antolin, P., et al. 2021, *Space Sci. Rev.*, 217, 73
- Nakariakov, V. M., Anfinogentov, S. A., Nisticò, G., & Lee, D. H. 2016, A&A, 591, L5
- Nakariakov, V. M. & Kolotkov, D. Y. 2020, ARA&A, 58, 441
- Nakariakov, V. M. & Ofman, L. 2001, A&A, 372, L53
- Nakariakov, V. M., Ofman, L., Deluca, E. E., Roberts, B., & Davila, J. M. 1999, *Science*, 285, 862
- Nakariakov, V. M. & Verwichte, E. 2005, *Living Reviews in Solar Physics*, 2, 3
- Nechaeva, A., Zimovets, I. V., Nakariakov, V. M., & Goddard, C. R. 2019, ApJS, 241, 31
- Nisticò, G., Nakariakov, V. M., & Verwichte, E. 2013, A&A, 552, A57
- Ofman, L. 2009, ApJ, 694, 502
- Ofman, L. & Wang, T. J. 2008, A&A, 482, L9
- Okamoto, T. J., Tsuneta, S., Berger, T. E., et al. 2007, *Science*, 318, 1577
- Pascoe, D. J., Wright, A. N., & De Moortel, I. 2010, ApJ, 711, 990
- Petrova, E., Magyar, N., Van Doorselaere, T., & Berghmans, D. 2023, ApJ, 946, 36
- Poedts, S. & Kerner, W. 1991, *Phys. Rev. Lett.*, 66, 2871
- Reale, F. 2014, *Living Reviews in Solar Physics*, 11, 4
- Roberts, B. 2019, *MHD Waves in the Solar Atmosphere* (Cambridge University Press)
- Robertson, D. & Ruderman, M. S. 2011, A&A, 525, A4
- Robertson, D., Ruderman, M. S., & Taroyan, Y. 2010, A&A, 515, A33
- Ruderman, M. S. 2003, A&A, 409, 287
- Ruderman, M. S. & Petrukhin, N. S. 2023, MNRAS, 523, 2074
- Ruderman, M. S., Petrukhin, N. S., & Pelinovsky, E. 2021, *Sol. Phys.*, 296, 124
- Ruderman, M. S. & Roberts, B. 2002, ApJ, 577, 475
- Sakurai, T., Goossens, M., & Hollweg, J. V. 1991, *Sol. Phys.*, 133, 227
- Schrijver, C. J. 2007, ApJ, 662, L119
- Schrijver, C. J., Aschwanden, M. J., & Title, A. M. 2002, *Sol. Phys.*, 206, 69
- Schrijver, C. J. & Brown, D. S. 2000, ApJ, 537, L69
- Schrijver, C. J., Title, A. M., Berger, T. E., et al. 1999, *Sol. Phys.*, 187, 261

- Sescu, A. 2015, *Advances in Difference Equations*, 2015, 1
- Sewell, G. 1988, *The Numerical Solution of Ordinary and Partial Differential Equations* (San Diego: Academic Press)
- Shi, M., Li, B., & Yuan, S. 2024, arXiv e-prints, arXiv:2402.11181
- Shi, M., Van Doorselaere, T., Guo, M., et al. 2021, *ApJ*, 908, 233
- Soler, R., Goossens, M., Terradas, J., & Oliver, R. 2013, *ApJ*, 777, 158
- Soler, R., Goossens, M., Terradas, J., & Oliver, R. 2014, *ApJ*, 781, 111
- Soler, R. & Luna, M. 2015, *A&A*, 582, A120
- Soler, R., Oliver, R., & Ballester, J. L. 2009, *ApJ*, 693, 1601
- Soler, R. & Terradas, J. 2015, *ApJ*, 803, 43
- Terradas, J., Andries, J., Goossens, M., et al. 2008a, *ApJ*, 687, L115
- Terradas, J., Arregui, I., Oliver, R., et al. 2008b, *ApJ*, 679, 1611
- Terradas, J., Oliver, R., & Ballester, J. L. 2005, *ApJ*, 618, L149
- Terradas, J., Oliver, R., & Ballester, J. L. 2006, *ApJ*, 642, 533
- Tian, H., McIntosh, S. W., Wang, T., et al. 2012, *ApJ*, 759, 144
- Tirry, W. J. & Goossens, M. 1996, *ApJ*, 471, 501
- Van Doorselaere, T., Andries, J., Poedts, S., & Goossens, M. 2004, *ApJ*, 606, 1223
- Van Doorselaere, T., Nakariakov, V. M., Young, P. R., & Verwichte, E. 2008a, *A&A*, 487, L17
- Van Doorselaere, T., Ruderman, M. S., & Robertson, D. 2008b, *A&A*, 485, 849
- Verwichte, E., Aschwanden, M. J., Van Doorselaere, T., Foullon, C., & Nakariakov, V. M. 2009, *ApJ*, 698, 397
- Verwichte, E., Nakariakov, V. M., Ofman, L., & Deluca, E. E. 2004, *Sol. Phys.*, 223, 77
- Verwichte, E., Van Doorselaere, T., White, R. S., & Antolin, P. 2013, *A&A*, 552, A138
- Wang, H. & Sakurai, T. 1998, *PASJ*, 50, 111
- Wang, T., Ofman, L., Davila, J. M., & Su, Y. 2012, *ApJ*, 751, L27
- Wang, T. J., Solanki, S. K., & Selwa, M. 2008, *A&A*, 489, 1307
- Watko, J. A. & Klimchuk, J. A. 2000, *Sol. Phys.*, 193, 77
- White, R. S. & Verwichte, E. 2012, *A&A*, 537, A49
- White, R. S., Verwichte, E., & Foullon, C. 2013, *ApJ*, 774, 104
- Williams, T., Walsh, R. W., & Morgan, H. 2021, *ApJ*, 919, 47
- Yi, Z., Engvold, O., & Keil, S. L. 1991, *Sol. Phys.*, 132, 63
- Yu, H., Li, B., Chen, S., & Guo, M. 2021, *Sol. Phys.*, 296, 95
- Zajtsev, V. V. & Stepanov, A. V. 1975, *Issledovaniia Geomagnetizmu Aeronomii i Fizike Solntsa*, 37, 3
- Zhong, S., Nakariakov, V. M., Kolotkov, D. Y., et al. 2023, *Nature Communications*, 14, 5298
- Zhong, S., Nakariakov, V. M., Kolotkov, D. Y., Verbeeck, C., & Berghmans, D. 2022, *MNRAS*, 516, 5989
- Zimovets, I. V. & Nakariakov, V. M. 2015, *A&A*, 577, A4

Appendix A: Subtleties with Domain Size and Grid Spacing

This appendix examines the influences that the numerical grid setup may have on our time-dependent solutions, taking two-circular-tube computations as examples. Our $[b, \bar{l}]$ notations are used together with the RR02 convention $[\mathcal{R}, \ell]$. It suffices to address only the S_x pattern for a fixed combination of physical parameters $[\rho_i/\rho_e = 5, \ell/\mathcal{R} = 0.4, d/\mathcal{R} = 2.5, kb = \pi/30]$.

We start with Fig. 13 by displaying the temporal evolution of the x -speed at the left tube center ($v_x(-d/2, 0; t)$, the solid curves) for a number of domain sizes $[x_M, y_M]$ as discriminated by the different colors. The best-fit damping envelopes are further plotted by the dashed curves for reference. All computations pertain to a fixed grid spacing $\Delta = 0.01b$, which is recalled to be different from the reference value in Table 1. Some differences are seen among the solid curves, the most prominent one being that the monochromatic cycles in the v_x signal are slightly delayed when the domain size increases. We find that this domain size effect arises because the zero-gradient boundary condition is not fully transparent to impinging motions initiated with the pair of planar perturbations given by Eq. (20). Some weakly reflected disturbances reach and interact with the composite structure, resulting in some longer time for the internal flow fields to settle toward a regular pattern for a larger domain. That the domain size effect is primarily attributed to the form of the initial perturbation is further corroborated by an additional series of computations where we multiply each exponential term in Eq. (20) by a factor $\exp(-y^2/b^2)$. The dependence on the domain size is then found to disappear in the time-dependent solutions responding to this localized perturbation. A monochromatic pattern remains clearly visible after some transitory phase, the period being nearly identical to what we find when Eq. (20) is employed. However, the damping envelope deviates considerably from an exponential one, making it difficult to examine ideal quasi-modes from an IVP perspective. The reasons for us to stick to Eq. (20) are twofold. Firstly, what drives the internal field toward a quasi-mode behavior is beyond our scope. Rather, we content ourselves with deriving the relevant periods and damping times. Secondly, varying the domain size does not influence the best-fit period (P_{fit}) and only marginally impacts the best-fit damping time (τ_{fit}). In fact, P_{fit} always evaluates to $\sim 112.5b/v_{\text{Ae}}$ for the examined domains. The value of $\tau_{\text{fit}}v_{\text{Ae}}/b$, on the other hand, changes from 320.1 for $[x_M = 12b, y_M = 10b]$ only modestly to 313.3 for $[x_M = 18b, y_M = 15b]$. An even weaker variation is found when the domain is further extended to $[x_M = 24b, y_M = 20b]$, in which case $\tau_{\text{fit}}v_{\text{Ae}}/b$ attains 314.3.

One may ask why we chose a spacing $\Delta = 0.01b$ different from the reference value ($\Delta = 0.005b$) when examining the domain size effect. The answer is that the specific values of Δ do not impact the $v_x(-d/2, 0; t)$ sequences for a given domain size if Δ is sufficiently small. By “sufficiently” we mean some criterion related to the pair of equilibrium quantities $[\rho_i/\rho_e, \bar{l}]$ (see Sect. 2.4). We reach this statement by varying only Δ for a substantial fraction of the computations in Fig. 4. Consider only those with the reference domain size. Figure 14 offers a representative case with $\ell/\mathcal{R} = 0.4$ by discriminating the $v_x(-d/2, 0; t)$ sequences for different Δ with the different linestyles. Relative to the computation with the reference Δ (the red dashed curve), no difference can be discerned when the spacing is halved (blue dash-dotted) or doubled (black dotted). The reference Δ is therefore overly demanding of computational resources for $\ell/\mathcal{R} = 0.4$, and the same can be said even for the most stringent case where $\ell/\mathcal{R} = 0.2$ provided that only $v_x(-d/2, 0; t)$ is of interest. That said, varying Δ necessarily entails differences in other aspects of the flow fields. We illustrate this point by fixing ℓ/\mathcal{R} again at 0.4 and implementing the reference domain size.

Figure 15 presents the spatial profiles of the x -speed along the y -cut through the left tube center at $t = 340b/v_{\text{Ae}}$. This instant is chosen rather arbitrarily to be marginally inside the interval where our fitting procedure is performed. A cut through a tube center, on the other hand, is chosen to ease the description of some key dynamics. A number of grid spacings are implemented and discriminated by the different colors. Only the lower half ($y \leq 0$) of a y -profile is displayed because the other half is symmetric with respect to $y = 0$. The vertical dash-dotted lines represent the borders of the nonuniform layer. Focus for now on this layer, where one sees a series of ripples in all computations. The most prominent effect associated with Δ is that the ripples are better resolved when the numerical grid gets finer, with the computed magnitudes of the local extrema being larger. Physically speaking, however, all computations prove capable of capturing the phase-mixing physics pertaining to the Alfvén continuum. To demonstrate this, we note that the Alfvén frequency $\omega_A = kv_A$ is locally symmetric about $x = -d/2$, meaning $\partial\omega_A/\partial x = 0$ for the chosen cut. It then follows from Mann et al. (1995) that the v_x profile in the layer can be written as

$$v_x \propto \mathcal{A}(y) \cos[\omega_A(y)t + \varphi_0], \quad (\text{A.1})$$

where $\mathcal{A}(y)$ is some slow-varying envelope. Let $\omega_{\text{Ai}} = kv_{\text{Ai}}$ be the internal Alfvén frequency. Some instantaneous phase variation $\phi_{\text{ac}}(t) = (\omega_{\text{Ae}} - \omega_{\text{Ai}})t$ is therefore accumulated over the continuum, leading to $N_{\text{hc}} = \lfloor \phi_{\text{ac}}(t)/\pi \rfloor$ half-cycles with $\lfloor \cdot \rfloor$ being the floor function (see Shi et al. 2024, for similar applications). Consequently, one expects N_{hc} or $N_{\text{hc}} + 1$ extrema, where the uncertainty derives from the phase φ_0 in Eq. (A.1). Plugging in the numbers yields a ϕ_{ac}/π of 6.27, and therefore 6 or 7 extrema are expected. This expectation is faithfully reproduced in Fig. 15. The same can actually be said for all instants when the internal field behaves like a quasi-mode. Now move on to the portions outside the nonuniform layer. The only difference that one can barely tell for different Δ appears in the external flow fields immediately adjacent to the layer. On the other hand, no difference can be discerned in the internal motions.

Figure 16 examines the grid spacing effect from the energetics perspective, differentiating Δ by the different colors. Equations (12) to (15) are employed to evaluate all energetics-related quantities, and we take the area Q therein to be a box $[-(d/2 + 1.2b), (d/2 + 1.2b)] \times [-1.2b, 1.2b]$. Figure 16a performs a gross energy balance analysis over Q by presenting the temporal profiles of the time-derivative of the instantaneous total energy (dE_{tot}/dt , the solid curves) and those of the instantaneous energy flux into Q ($-F$, asterisks). The asterisks of different colors cannot be told apart, the reason being that all computations yield an identical set of dependents at the boundaries of Q . Some difference nonetheless shows up among the solid curves, despite that dE_{tot}/dt should balance F (see Eq. 12). As intuitively expected, gross energy conservation is maintained for a longer duration when a finer grid is employed, with some $\sim 30\%$ difference between dE_{tot}/dt and $-F$ staring to appear at $t \sim 90b/v_{\text{Ae}}$ ($\sim 270b/v_{\text{Ae}}$) when $\Delta = 0.01b$ ($0.0025b$). Note that the examined Q is the union of three mutually exclusive portions, namely the tube interiors (to be denoted as “int”), nonuniform layers (“layer”), and exterior (“ext”). Figure 16b then displays, against time, the energies in these individual

portions. By far the most significant effect that the grid spacing has on the energetics is that the energy in the nonuniform layer is increasingly under-estimated when Δ increases. However, there exists only some weak difference among the E_{ext} curves because only the flows in the immediate neighborhood of either tube are somehow impacted by choices of Δ . Furthermore, the internal energies (E_{int}) consistently remain the same when Δ is varied, reinforcing the notion that Δ has no influence on the internal flow field.

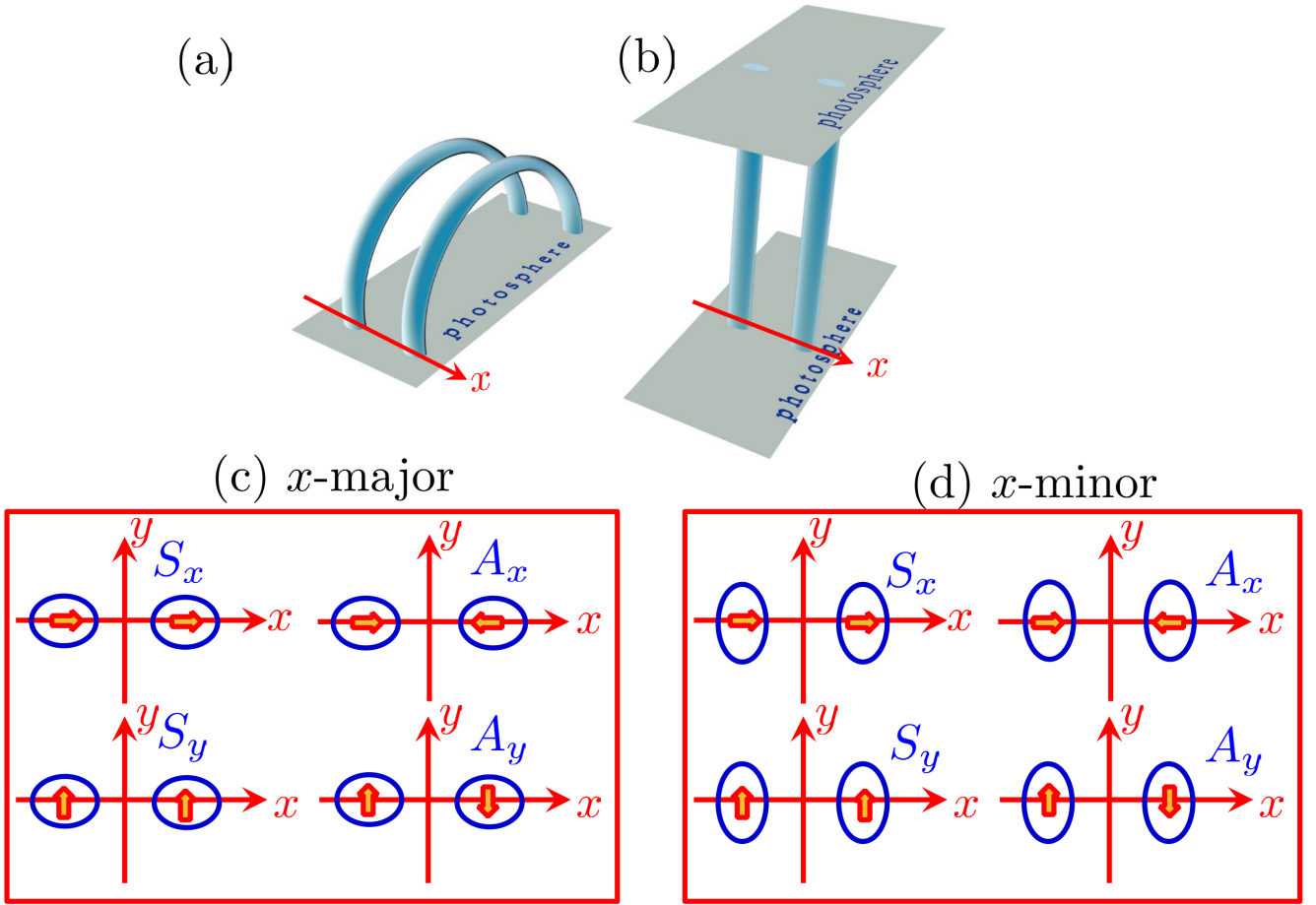


Fig. 1. Schematics showing both the two-elliptic-tube configuration and lower-order kink motions therein. Illustrated in (b) are two identical tubes with elliptic cross-sections and separated in the x -direction. The $y - z$ plane is identified as the tube plane, the meaning of which is clearer in the curved representation in panel a. This study examines only two tube orientations (panels c and d), with the one labeled “ x -major” (“ x -minor”) corresponding to the situation where the major- (minor-)axis of either tube is aligned with the x -axis. The tube centers are placed symmetrically with respect to the y -axis. Only axial fundamentals are considered, making it possible to examine the three-dimensional (3D) wave fields with a 2D approach. Lower-order kink motions are classified according to their internal flow fields in the apex plane (panels c or d); hence such symbols as S_x and A_y . See text for more details.

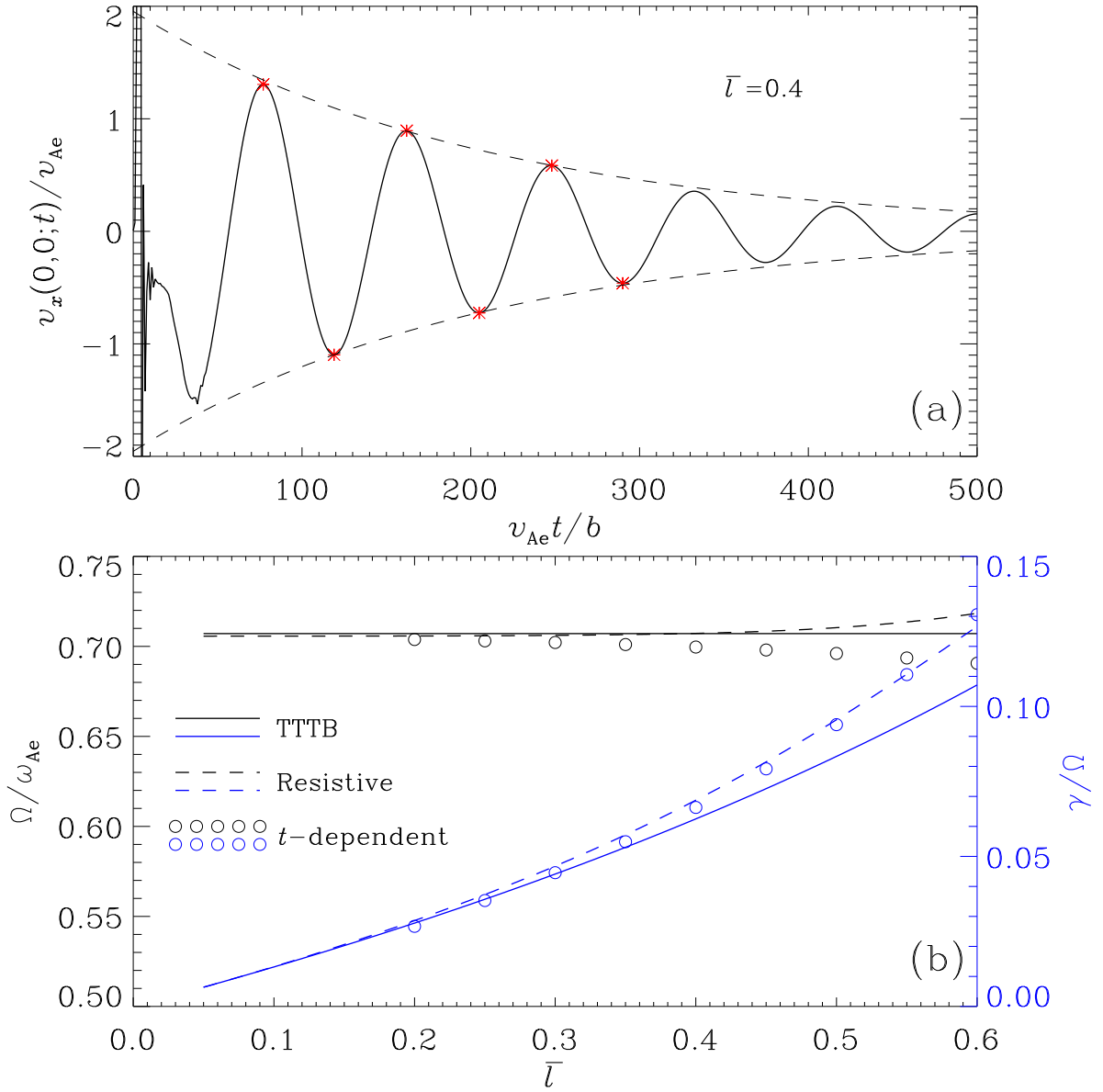


Fig. 2. Kink motions in isolated tubes with circular cross-sections for a fixed pair of density contrast and dimensionless axial wavenumber [$\rho_i/\rho_e = 3, kb = \pi/30$]. A specific dimensionless layer width $\bar{l} = 0.4$ is examined in (a), the solid curve showing the x -speed sampled at the tube center ($v_x(0,0,t)$). An exponentially damped cosine is employed to fit the segment encompassing the extrema shown by the red asterisks, with the resulting damping envelope plotted over the entire interval (the dashed curves). Presented in (b) are the \bar{l} -dependencies of the mode frequencies (Ω , the black curves and symbols) and the ratios of the decay rate to the frequency (γ/Ω , blue) obtained with various methods. The solid curves represent the analytical thin-tube-thin-boundary (TTTB) expectations with Eq. (25). No assumption on tube length or layer width is imposed in the “Resistive” computations (the dashed curves) that evaluate ideal quasi-modes as resistive eigenmodes. Shown by the open circles are the best-fit results from our time-dependent computations, where kink motions are consistently excited with a perturbation given by Eq. (26).

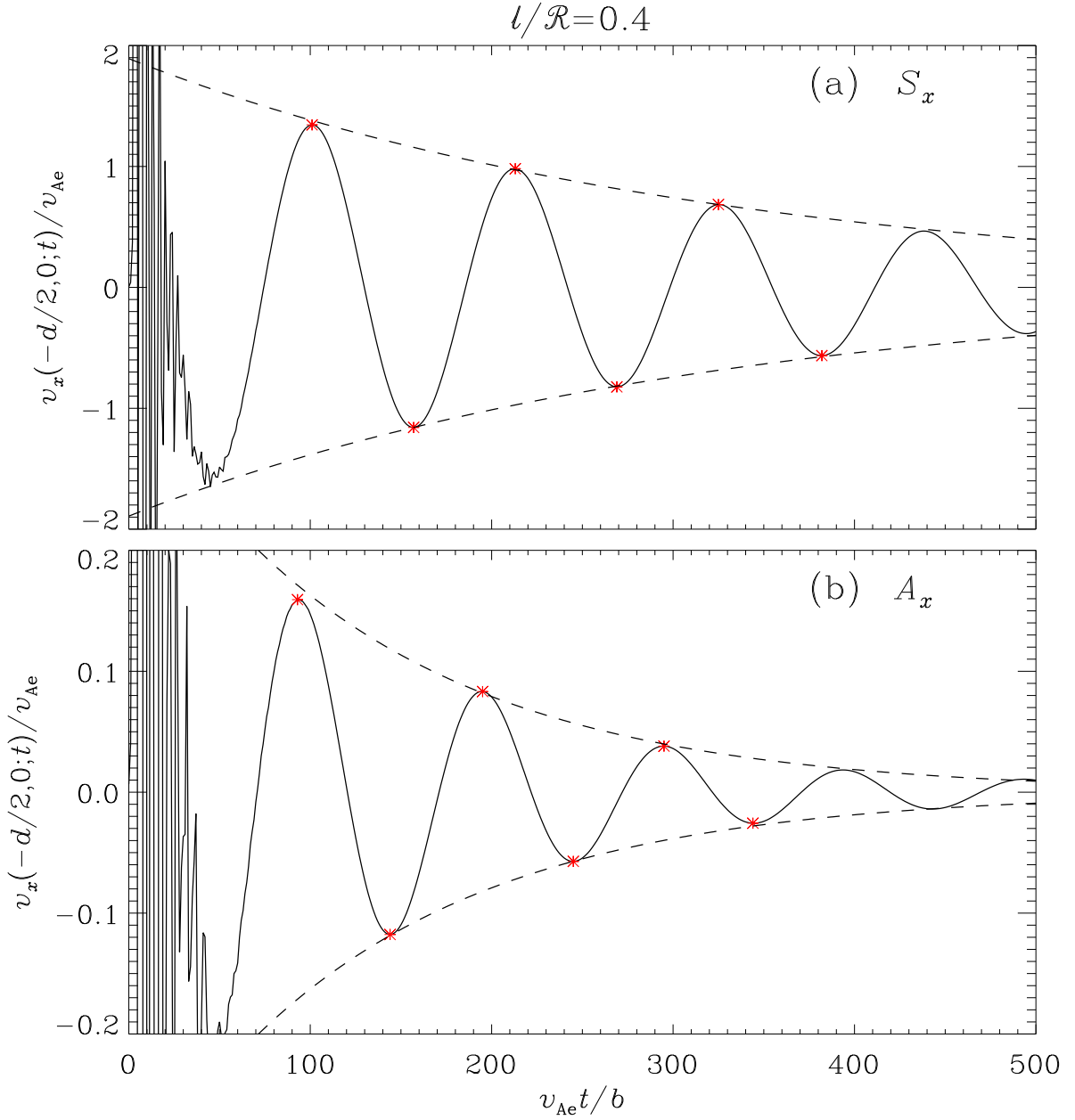


Fig. 3. Kink motions with (a) S_x and (b) A_x patterns in a two-circular-tube configuration. Plotted are the time sequences of the x -speed sampled at the left tube center ($v_x(-d/2, 0; t)$, the solid curves) together with the best-fit damping envelopes (dashed). The time-dependent computations pertain to a fixed combination $[\rho_i/\rho_e = 5, \ell/\mathcal{R} = 0.4, d/\mathcal{R} = 2.5, kb = \pi/30]$, with ℓ and \mathcal{R} being the nonuniform layer width and mean tube radius implemented by Ruderman & Roberts (2002). A fitting procedure with an exponentially damped cosine is performed over the duration exactly encompassing the extrema indicated by the red asterisks, even though the best-fit envelopes are plotted for the entire time interval. Kink motions are excited with the perturbation described by Eq. (20) with appropriate signs.

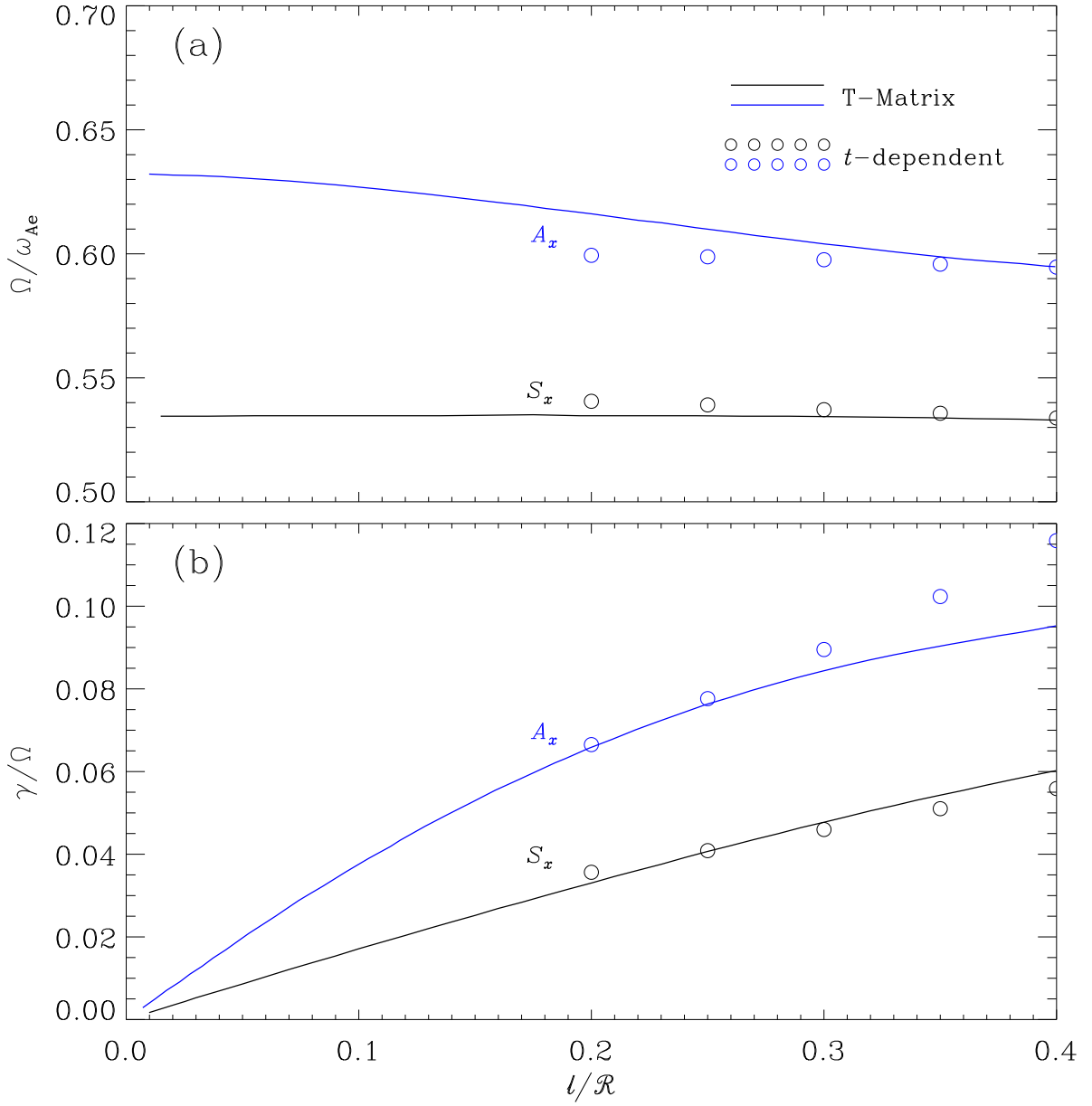


Fig. 4. Comparison of (a) the oscillation frequencies Ω and (b) damping rates γ of ideal quasi-modes deduced from time-dependent computations (the open circles) with those expected with the T-matrix formalism (solid lines). With different colors we discriminate the results for the S_x and A_x patterns. The T-matrix curves are read from Fig. 4 of Soler & Luna (2015, SL15). Shown here is how Ω and γ/Ω depend on l/\mathcal{R} , while the rest of the parameters is fixed at $[\rho_i/\rho_e = 5, d/\mathcal{R} = 2.5, kb = \pi/30]$. The $[l/\mathcal{R}, d/\mathcal{R}]$ notations follow from SL15 for the ease of comparison.

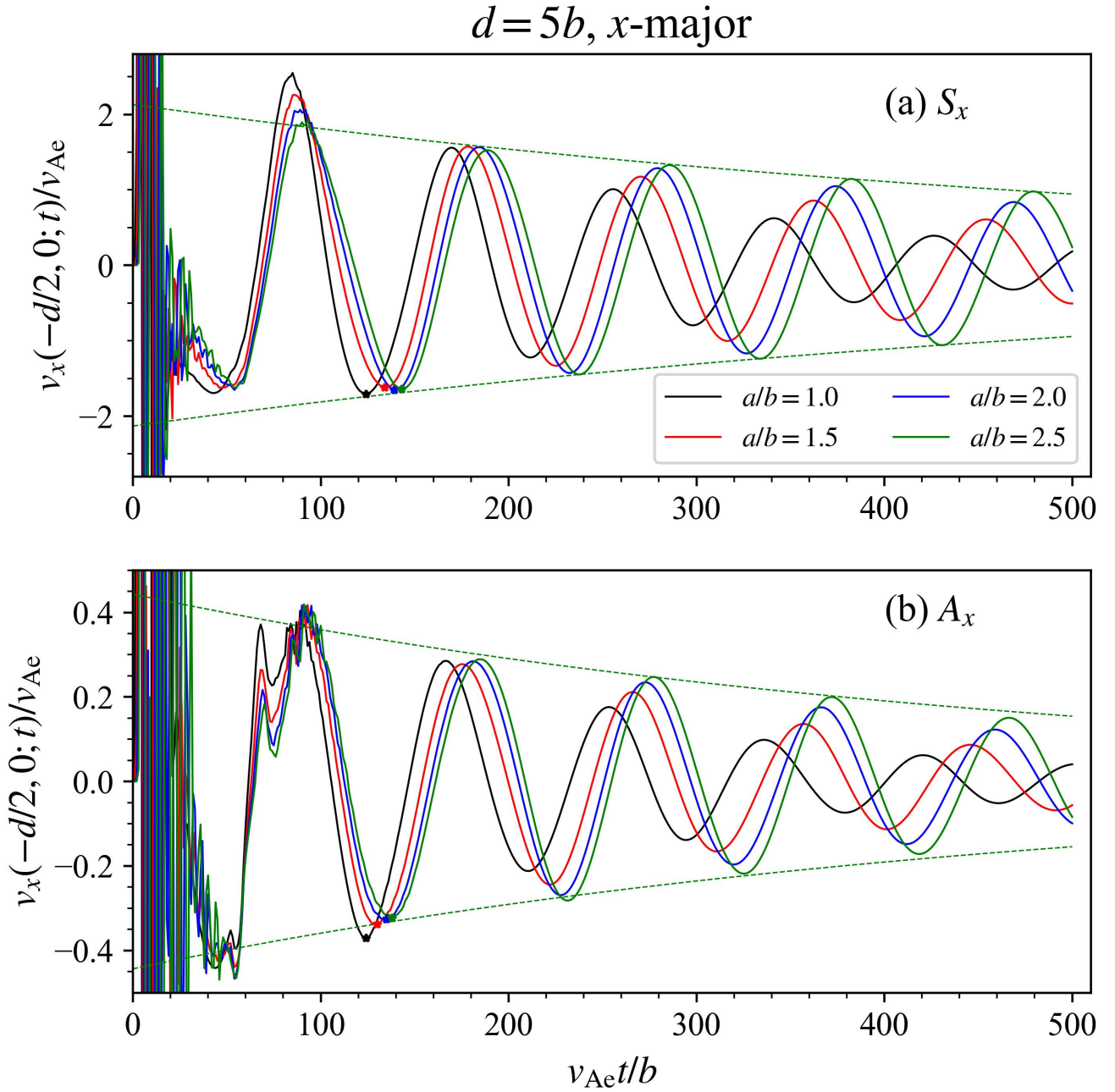


Fig. 5. Kink motions with (a) S_x and (b) A_x patterns in a two-elliptic-tube configuration with x -major orientation. Plotted are the time sequences of the x -speed sampled at the left tube center ($v_x(-d/2, 0; t)$, the solid curves) for a number of ratios of the semi-major to semi-minor axis (a/b) as discriminated by the different colors. A fitting procedure is performed, for each sequence, over the duration encompassing the six extrema starting with the one denoted by an asterisk. The best-fit damping envelope is plotted for the entire sequence, but only for $a/b = 2.5$ to avoid over-crowding the plots. The computations pertain to a fixed combination $[\rho_i/\rho_e = 3, \bar{l} = 0.4, d/b = 5, kb = \pi/30]$.

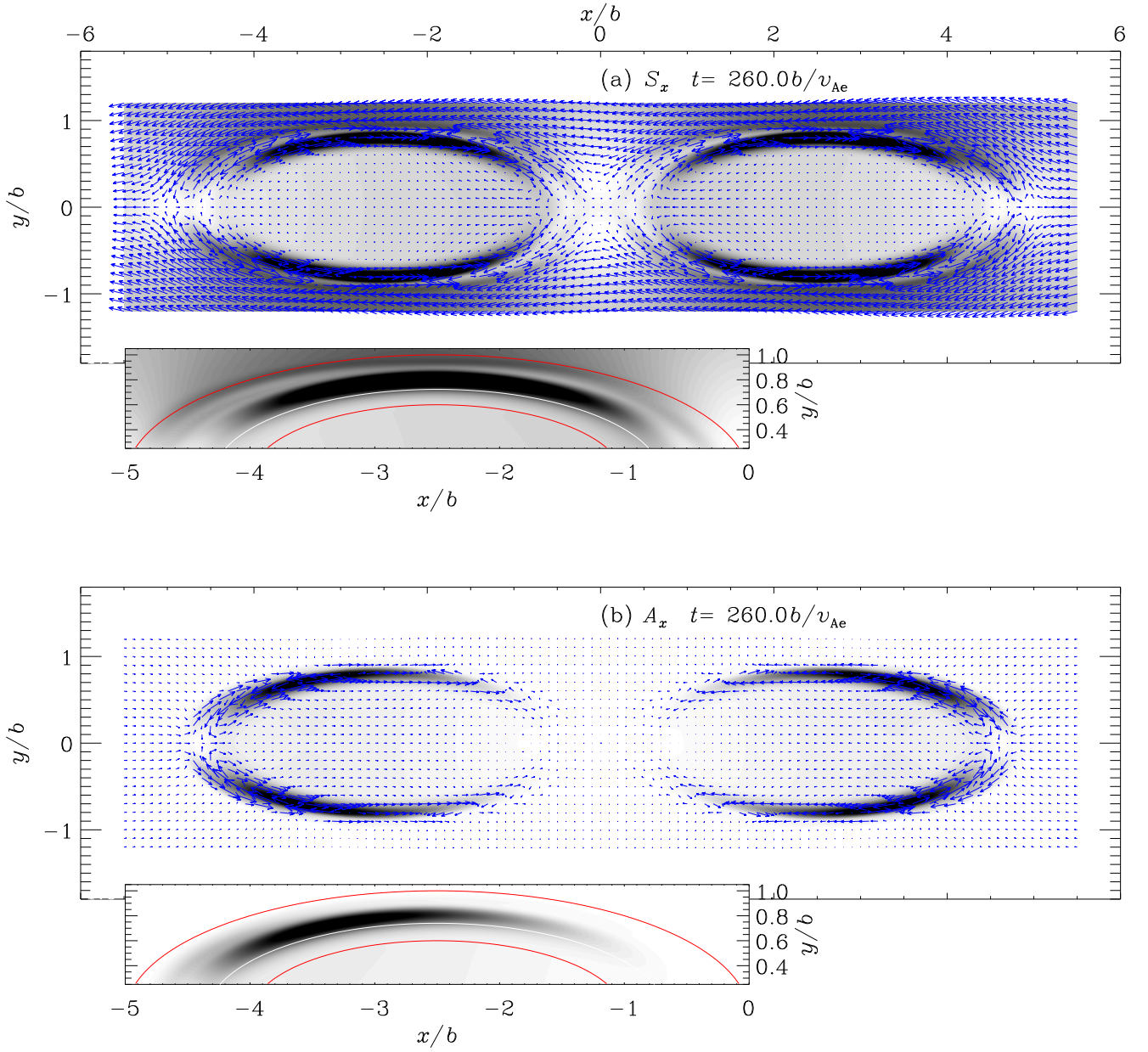


Fig. 6. Representative snapshots of the velocity field (the blue arrows) and energy density distribution (ϵ , filled contours) for (a) the S_x motion and (b) the A_x one in a two-elliptic-tube configuration with the x -major orientation. The inset in each panel emphasizes the distribution of ϵ in a representative nonuniform layer, whose boundaries are shown by the red solid curves. The white contour indicates where the Alfvén frequency $\omega_A = kv_A$ equals the quasi-mode frequency deduced with the fitting procedure. Both computations pertain to a fixed combination $[\rho_i/\rho_e = 3, a/b = 2.5, \bar{l} = 0.4, d/b = 5, kb = \pi/30]$. This snapshot is extracted from the animation attached to the current figure. The ϵ contours in all snapshots are filled in such a way that darker portions correspond to larger ϵ . The blue arrows are also consistently scaled in all snapshots such that longer arrows correspond to stronger velocities.

$a/b = 2.5$, $d = 5b$, x -major

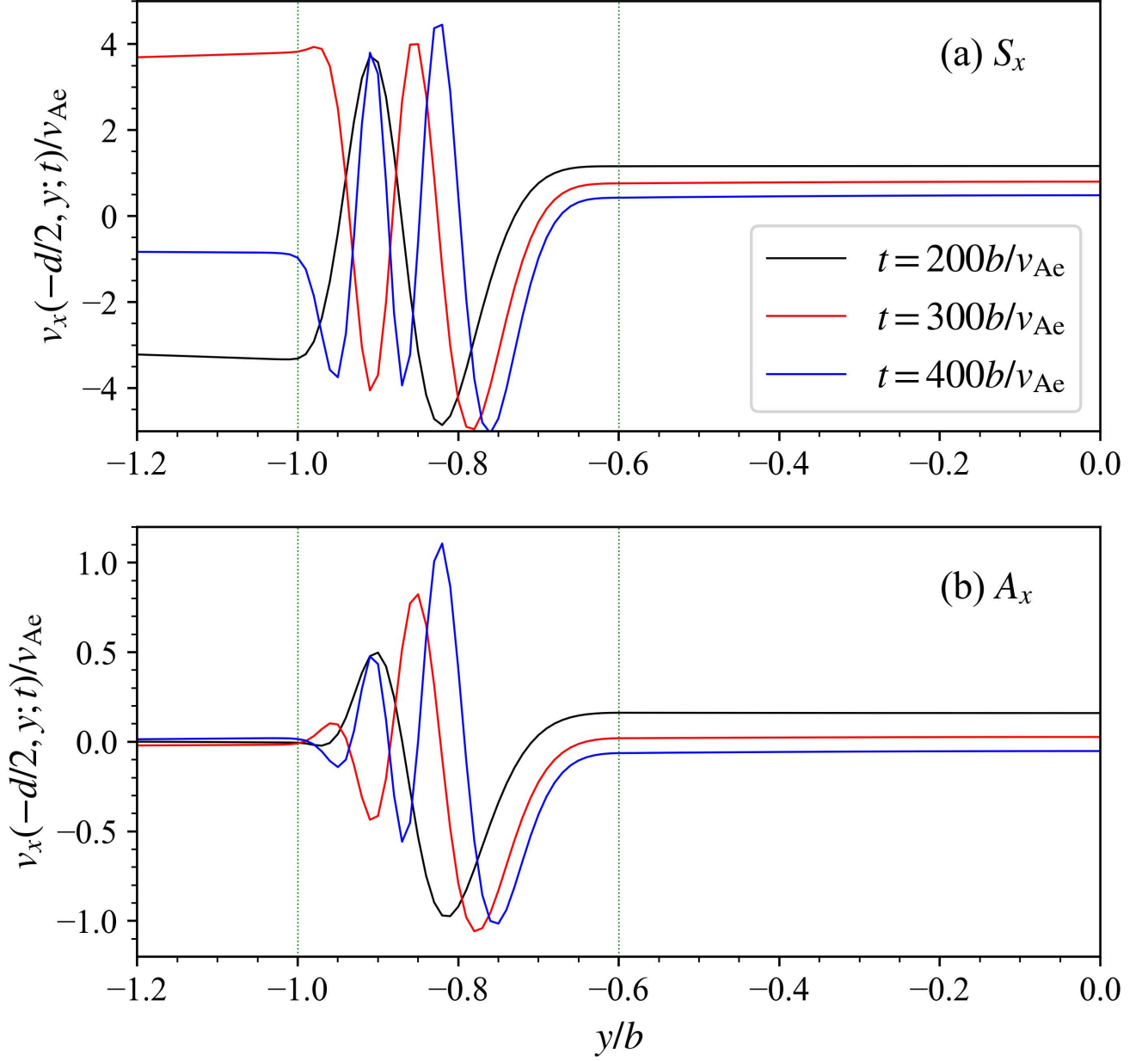


Fig. 7. Distributions of the x -speed along the y -cut through the left tube center at a number of instants as labeled. Panels (a) and (b) correspond to the S_x and A_x motions, respectively. The vertical dotted lines represent the borders of the nonuniform layer. Only the lower half ($y < 0$) of a y -profile is displayed, the other half being symmetric with respect to $y = 0$. All computations are conducted for the x -major orientation with a fixed combination of physical parameters [$\rho_i/\rho_e = 3$, $\bar{l} = 0.4$, $d/b = 5$, $kb = \pi/30$].

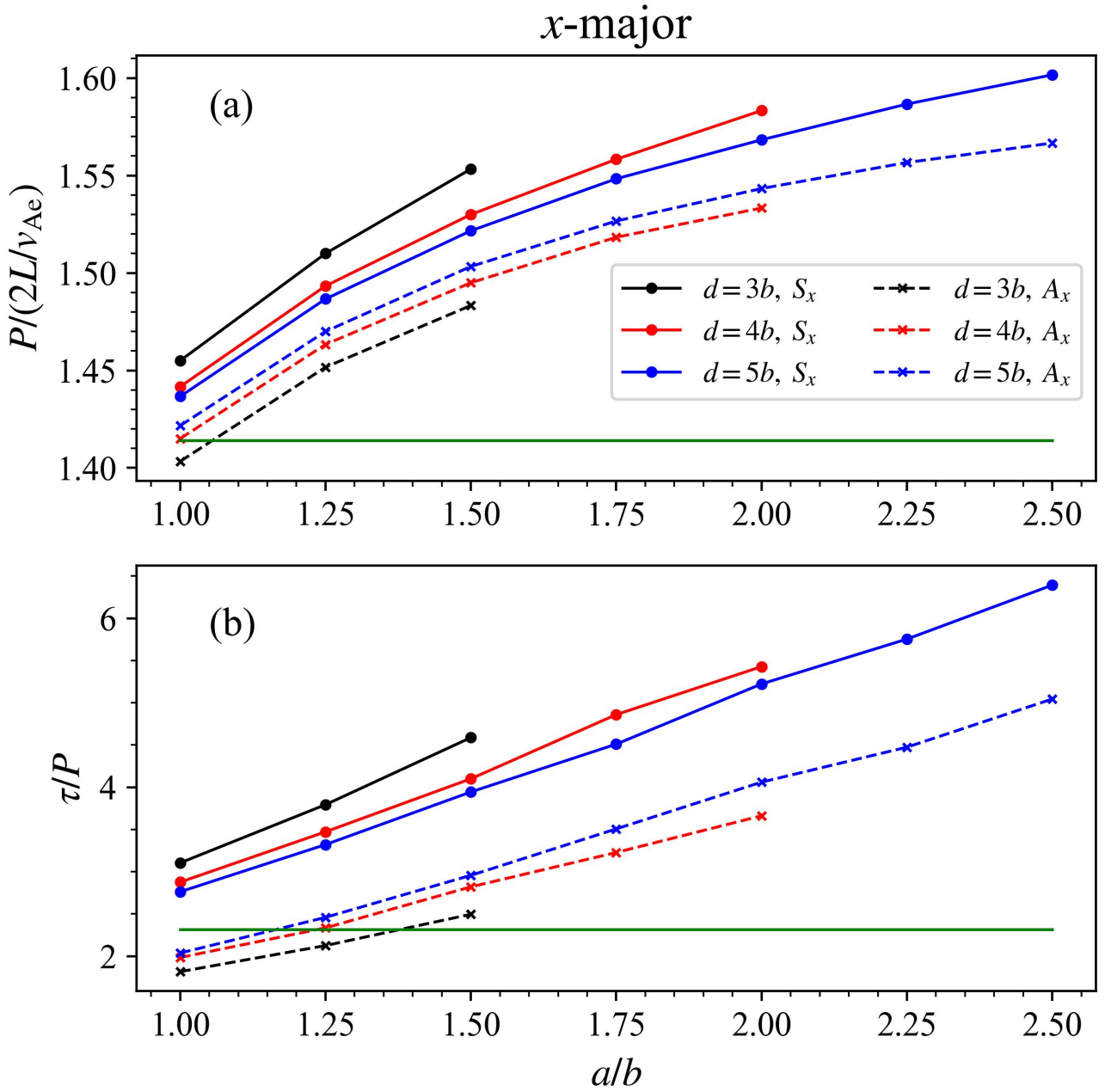


Fig. 8. Dependencies of (a) the quasi-mode periods (P) and (b) damping-time-to-period ratios (τ/P) on the ratio of semi-major to semi-minor axis (a/b) for kink motions in a two-elliptic-tube configuration with the x -major orientation. The S_x and A_x patterns are discriminated by the linestyles. A number of dimensionless tube separations (d/b) are examined as differentiated by the different colors, with d/b constrained to avoid tube overlapping. All results pertain to a fixed combination of physical parameters [$\rho_i/\rho_e = 3$, $\bar{l} = 0.4$, $kb = \pi/30$]. The horizontal lines represent the results for an isolated circular tube with the same set of parameters.

$d = 5b$, x -minor

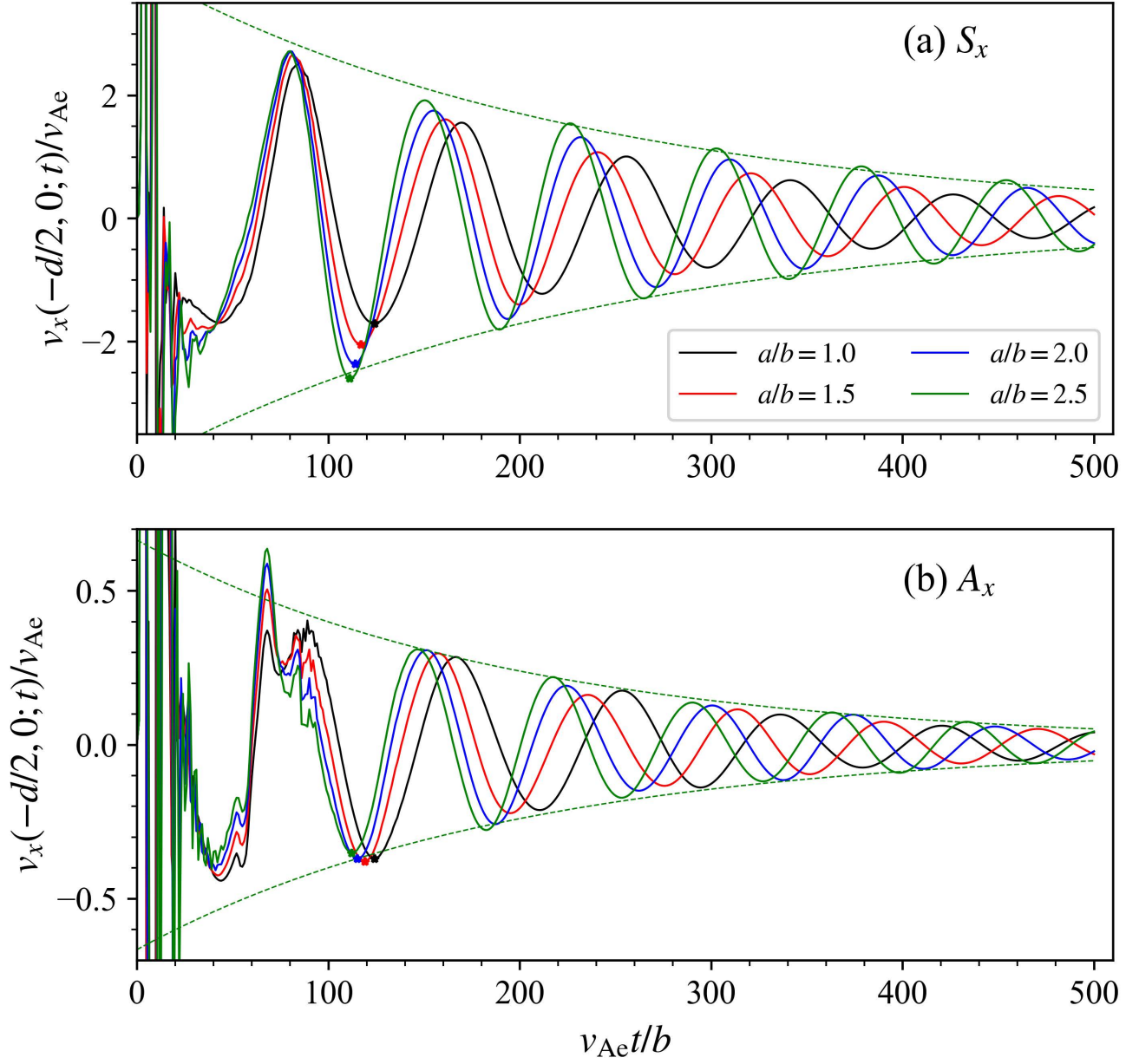


Fig. 9. Similar to Fig. 5 but for the x -minor orientation.

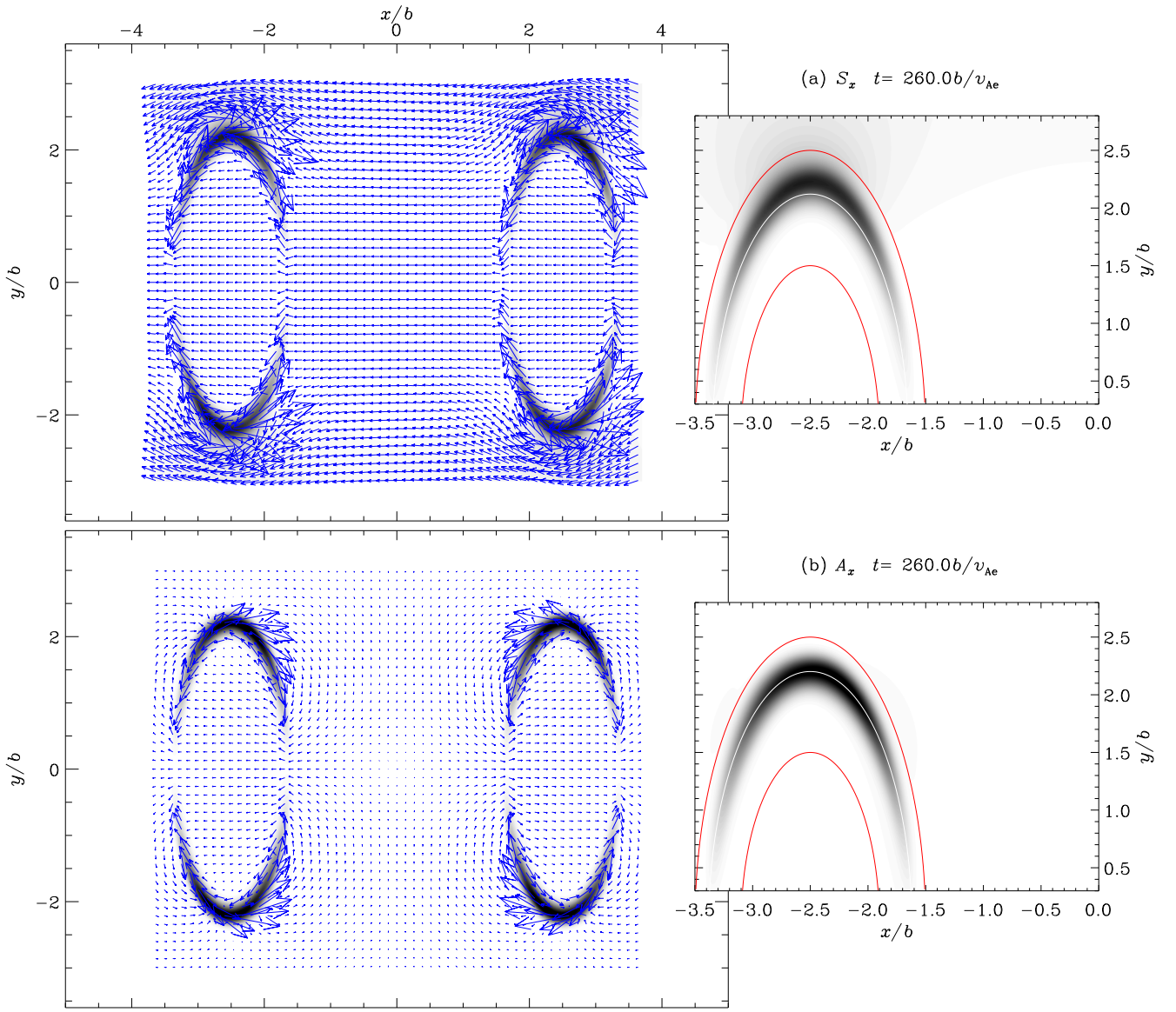


Fig. 10. Similar to Fig. 6 but for the x -minor orientation. The associated animation is also attached.

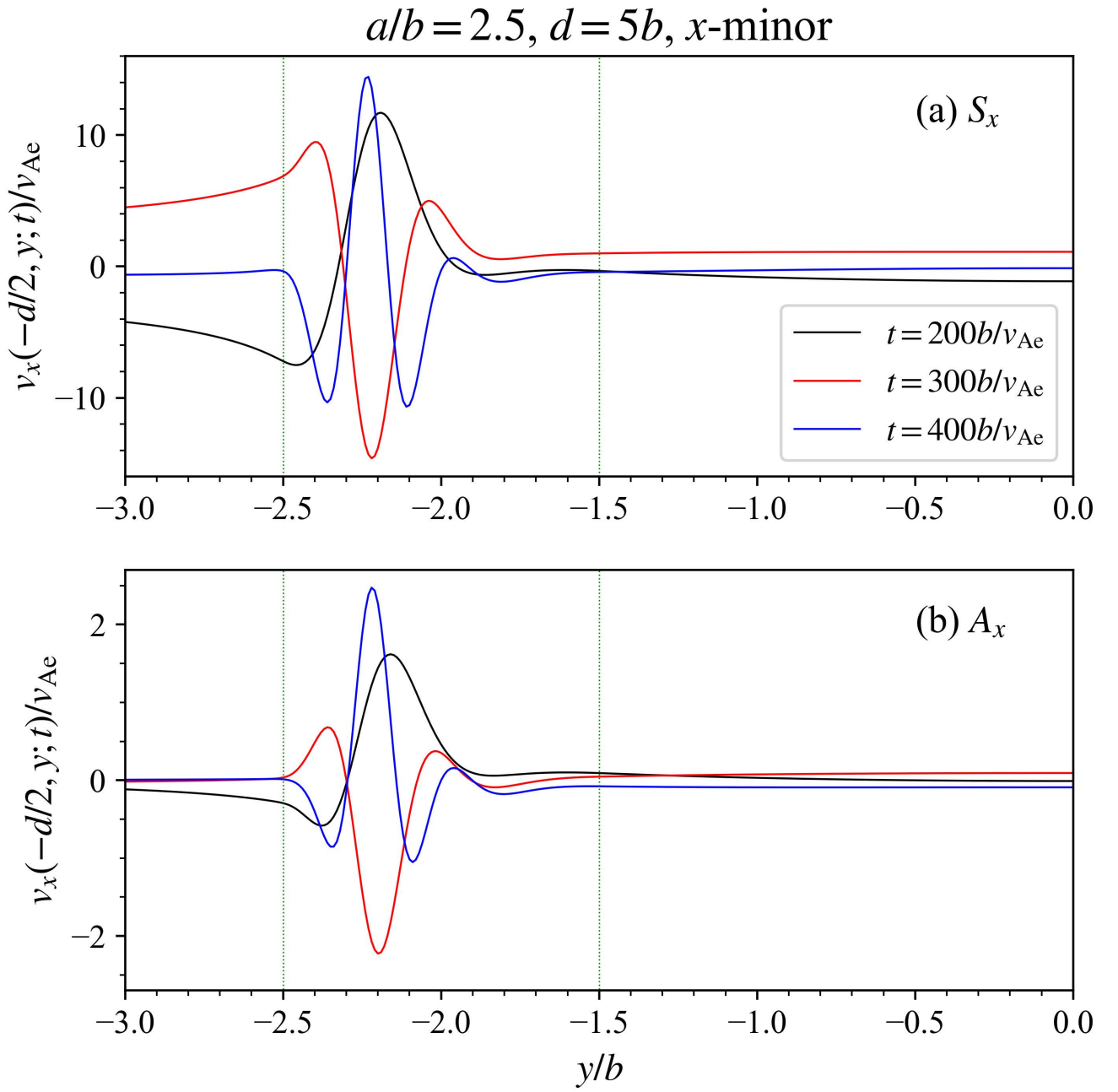


Fig. 11. Similar to Fig. 7 but for the x -minor orientation.

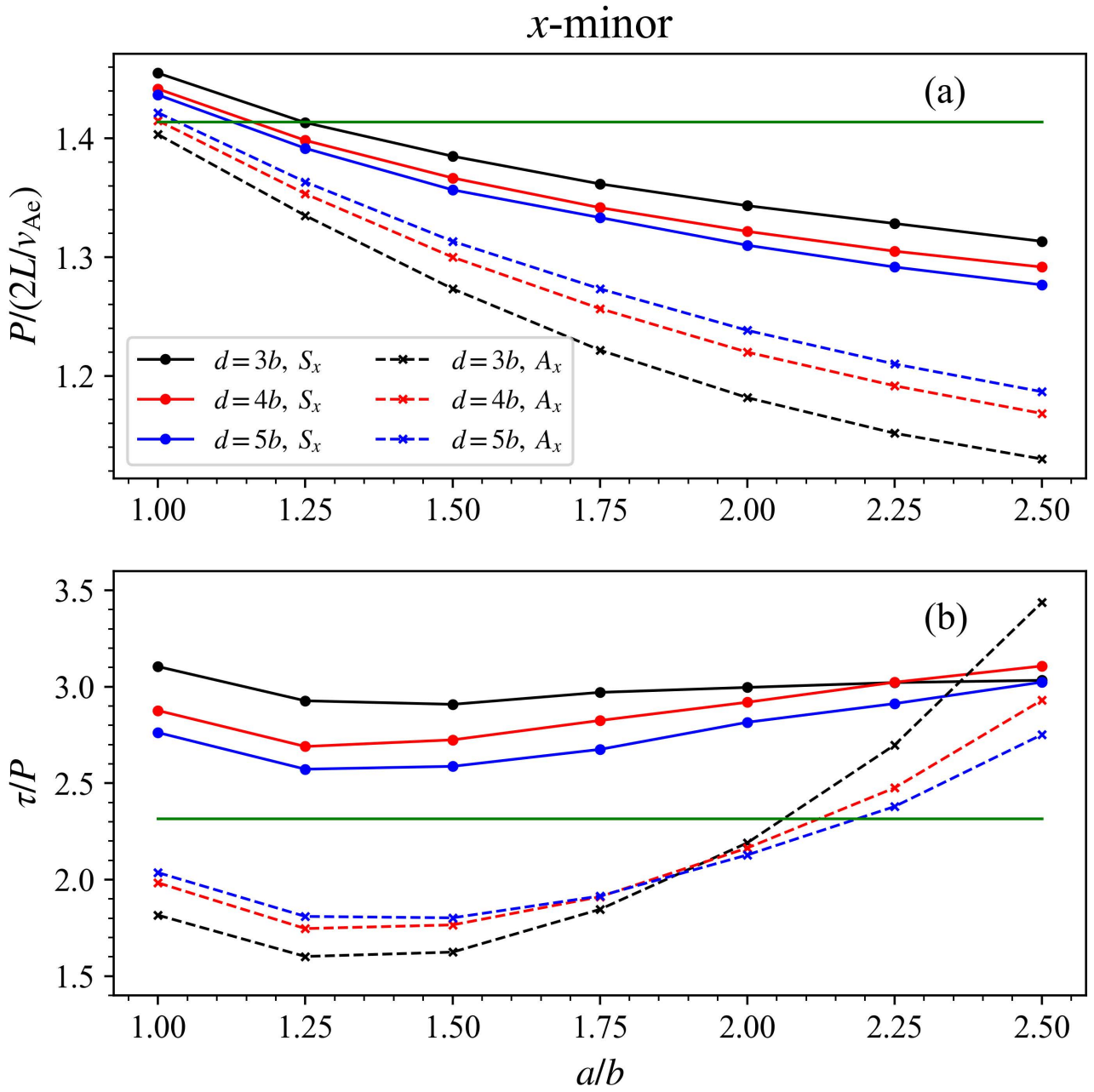


Fig. 12. Similar to Fig. 8 but for the x -minor orientation.

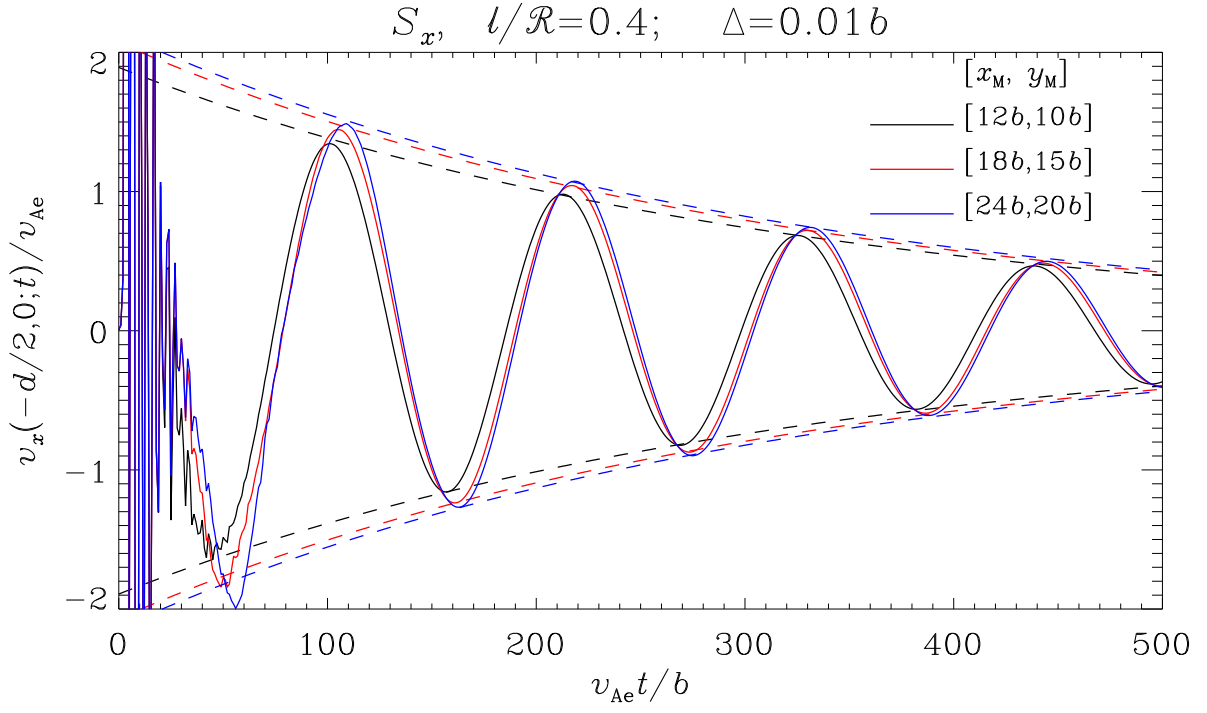


Fig. 13. Temporal profiles of the x -speed sampled at the left tube center ($v_x(-d/2, 0; t)$, the solid curves) for a number of domain sizes as labeled. Overplotted by the dashed curves are the best-fit damping envelopes. All computations pertain to the S_x motion for a fixed combination of physical parameters [$\rho_i/\rho_e = 5, \ell/\mathcal{R} = 0.4, d/\mathcal{R} = 2.5, kb = \pi/30$]. The grid spacing is fixed at $\Delta = 0.01b$.

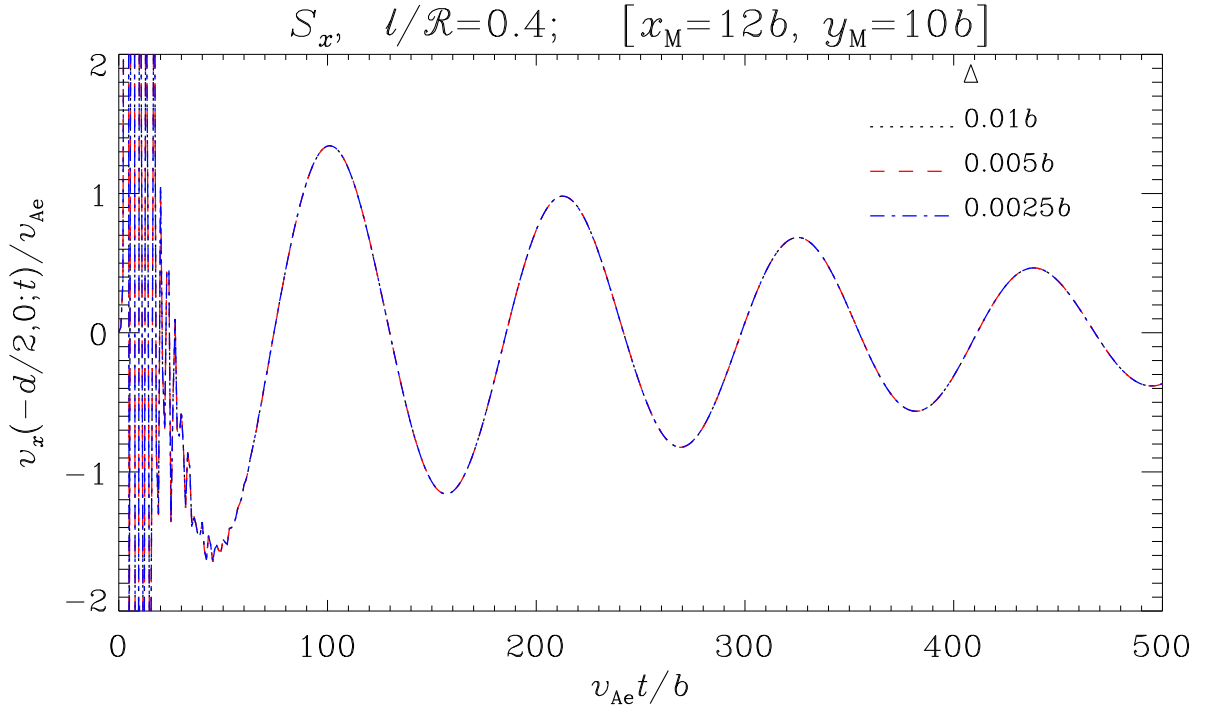


Fig. 14. Temporal profiles of the x -speed sampled at the left tube center for a number of grid spacings as labeled. All computations pertain to the S_x motion for a fixed combination of physical parameters $[\rho_i/\rho_e = 5, \ell/\mathcal{R} = 0.4, d/\mathcal{R} = 2.5, kb = \pi/30]$. The computational domain size is fixed at $[x_M = 12b, y_M = 10b]$.

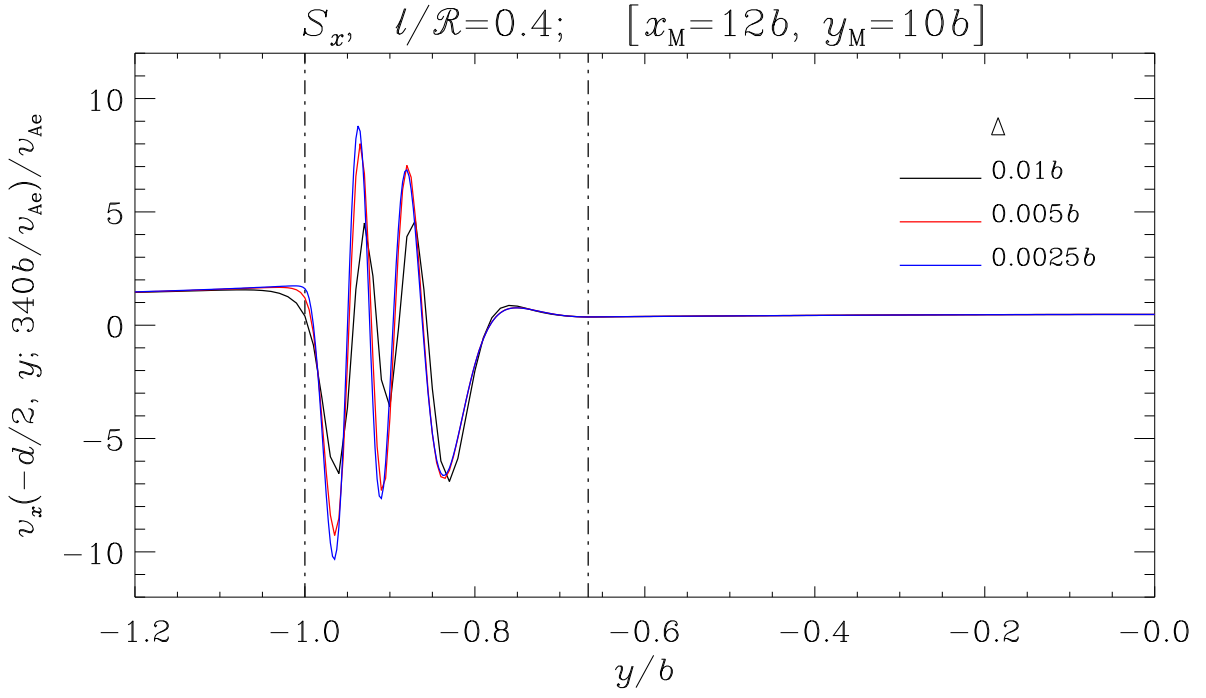


Fig. 15. Distributions of the x -speed at $t = 340b/v_{\text{Ae}}$ along the y -cut through the left tube center for a number of grid spacings as labeled. All computations pertain to the S_x motion for a fixed combination of physical parameters [$\rho_i/\rho_e = 5, \ell/\mathcal{R} = 0.4, d/\mathcal{R} = 2.5, kb = \pi/30$]. The computational domain size is fixed at $[x_M = 12b, y_M = 10b]$. Only the lower half ($y \leq 0$) is shown for any y -profile, the other half being symmetric about $y = 0$. The vertical dash-dotted lines delineate the borders of the nonuniform layer.

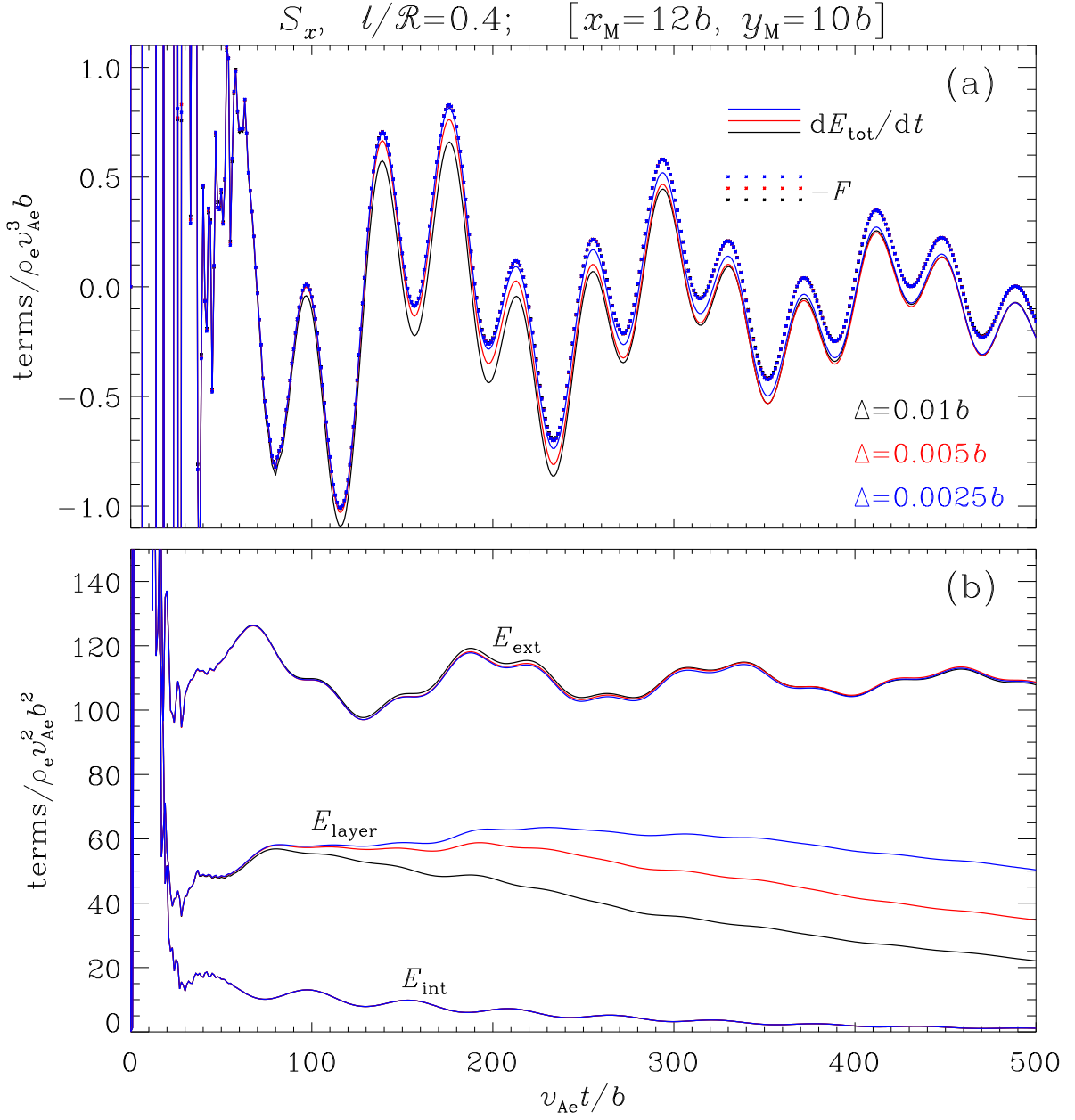


Fig. 16. Temporal profiles of some energetics-related quantities for several grid spacings as differentiated by different colors. Energetics are consistently examined for a box $[-(d/2 + 1.2b), (d/2 + 1.2b)] \times [-1.2b, 1.2b]$, in which the three mutually exclusive constituents are the tube interiors, nonuniform layers, and exterior. Shown in (a) are the time derivative of the total perturbation energy in the box (dE_{tot}/dt , the solid curves), together with the instantaneous energy flux into this box ($-F$, asterisks). Further plotted in (b) are the instantaneous total energy in the interiors (E_{int}), nonuniform layers (E_{layer}), and the exterior (E_{ext}). All computations pertain to the S_x pattern for a fixed combination of physical parameters $[\rho_i/\rho_e = 5, \ell/\mathcal{R} = 0.4, d/\mathcal{R} = 2.5, kb = \pi/30]$. The computational domain size is fixed at $[x_M = 12b, y_M = 10b]$.